Dysregulation of cholesterol and bile acid homeostasis in the gut-liver axis following *Cryptosporidium* intestinal infection

Shuhong Wang[1], Ai-Yu Gong[1], Edward Barker[1], David L. Williams[1], Christopher Forsyth[2], Liqing Yu[3], and Xian-Ming Chen[1,4]

[1]Department of Microbial Pathogens and Immunity, Rush University Medical Center, Chicago, Illinois, USA; [2]Department of Anatomy and Cell Biology, Rush University Medical Center, Chicago, Illinois, USA; [3]Division of Endocrinology, Diabetes and Nutrition, Department of Medicine, University of Maryland School of Medicine, Baltimore, Maryland 21201, USA.

[4]Correspondence: xian_m_chen@rush.edu

Abstract

Cryptosporidium spp., an apicomplexan protozoan, is one of the most common pathogens causing moderate-to-severe diarrhea in children under 2 years of age and is also an important opportunistic pathogen for patients with AIDS. There are currently no effective vaccines or therapies available. Infection in children is associated with malnutrition, growth defects, and even impaired cognitive development, but underlying mechanisms remain unclear. We report here that *C. parvum* infection in neonatal mice impairs bile acid reabsorption in the ileum, disrupts lipid metabolism in the liver, and alters bile acid homeostasis in the enterohepatic circulation. The reduction of bile acid pool further impairs lipid absorption in the small intestine. Additionally, replenishing bile prevents the decline in lipid absorption in infected neonatal mice. Strikingly, bile gavage significantly reduces the infection burden and ameliorates the dysregulated homeostasis of cell proliferation and migration in intestinal epithelium following infection. These findings may guide novel therapeutic approaches for cryptosporidiosis.

Introduction

Cryptosporidium is a significant opportunistic intestinal pathogen for immunocompromised individuals and one of the leading causes of moderate-to-severe diarrhea in children under 2 years of age[1]. Infection with this parasite in young kids is associated with mortality, growth stunting, and developmental deficits[2]. Recent estimates from the Global Burden of Diseases, Injuries, and Risk Factors Study (GBD) indicate *Cryptosporidium* spp. is responsible for approximately 7.6 million cases and between 48,000 and 202,000 deaths annually among young children in low-resource settings[3,4]. Cryptosporidiosis in humans is primarily caused by *C. parvum* and *C. hominis* species[2]. Nitazoxanide, the only approved drug for the treatment of cryptosporidiosis, is ineffective in immunocompromised patients and malnourished children[2,5–7]. Pathologically, *Cryptosporidium* infections are primarily confined to the distal ileum and it is speculated that the combined loss of microvillus borders and villus height reduces the absorptive surface area of the intestine, leading to diarrhea and malnutrition in children[8]. However, the current understanding of the underlying molecular mechanisms of malnutrition remains unclear, hampering the development of effective therapeutics. The intestinal mucosa consists of a monolayer of rapidly self-renewing epithelial cells. Intestinal stem cells in the crypts generate new functional epithelial cells, which mature and differentiate as they move up the villus before being shed at the tip[9,10]. *Cryptosporidium* infection is confined to the villi (mainly enterocytes) of the intestinal epithelium, where the organism forms an intracellular yet extra-cytoplasmic parasitophorous vacuole at the brush border following cell entry[11]. Increased cell death during infection triggers crypt hyperplasia and branching due to accelerated cell division to compensate for the loss of cells at the villi[8,12], however, its underlying molecular mechanisms remain unknown.

As a major source of nutrition for infants, milk provides a significant amount of fatty acids, phospholipids, and cholesterol. Bile acids are amphipathic molecules synthesized from cholesterol in the liver, stored in the gallbladder, and released into the duodenum after a meal[13]. Bile acids facilitate the emulsification of insoluble lipids into tiny mixed micelles, promoting lipid digestion and absorption in the intestine[14]. More than 95% of the bile acids are reabsorbed in the terminal ileum through the apical sodium-dependent bile salt transporter (ASBT; SLC10A2) and recirculated to the liver via the portal blood in a process known as enterohepatic circulation[13]. Bile acids have been identified as endogenous ligands with high affinity for the

Farnesoid X receptor (FXR), a ligand-activated transcription factor in the nuclear receptor (NR)-family [15–17]. Thus, the Bile acid-FXR network plays a crucial role in maintaining whole-body bile acid homeostasis by regulating the expression of target genes involved in both hepatic bile acid synthesis and enterohepatic circulation[18]. Using a murine neonatal infection model, we report that *Cryptosporidium* infection significantly disrupts bile acid and lipid homeostasis in both the intestine and liver. Functionally, bile intervention greatly reduces the infection burden, enhances intestinal lipid absorption, and ameliorates dysregulated intestinal homeostasis. These findings suggest that bile intervention may have therapeutic potential for intestinal cryptosporidiosis.

Results

C. parvum infection disrupts cholesterol homeostasis in the small intestine

Cryptosporidium lacks the capability to synthesize cholesterol and needs to acquire it both from the gut lumen and the host cell to meet its metabolite[19,20]. Therefore, we investigated whether *C. parvum* infection affects intestinal cholesterol absorption and transport. To explore this, we performed RNA-seq analysis to examine genome-wide changes in gene expression in the ileal epithelium of infected neonatal mice. Consistent with results from previous studies[21], RNA-Seq analysis of the ileal epithelium from infected neonatal mice [5-days old, 72 h post-infection (p.i.)] reveals significant changes in host gene expression (Supplementary Table 1). Gene set enrichment analysis (GSEA) indicates marked alterations in pathways related to inflammatory responses (Extended Data Fig. 2b), defense response (Extended Data Fig. 2c), and the regulation of sterol homeostasis in the infected ileum epithelium (Extended Data Fig. 2d).

Cellular cholesterol homeostasis is finely regulated through the dynamic balance between biosynthesis, uptake, export, and esterification[22]. The regulation of cellular cholesterol transport involves low-density lipoprotein receptor (LDLR)-mediated absorption and chylomicron secretion, as well as transmembrane influx/efflux through transporters such as Niemann-Pick C1-Like 1 (NPC1L1), the heterodimeric ATP-binding cassette transporters G5 and G8 (ABCG5/G8), and ATP-binding cassette transporter A1 (ABCA1) (Fig. 1a). This process is governed by intricate feedback regulation mechanisms, including the liver X receptor (LXR) signaling[23]. Further GSEA analysis indicates that cholesterol efflux, import, and esterase activity were significantly downregulated in the infected ileal epithelium (Fig. 1b and Extended Data Fig. 2a,d), while most genes involved in cholesterol biosynthesis were upregulated (Fig. 1b). Specifically, reduced expression of several cholesterol efflux genes, including ABCG5, ABCG8 and ABCA1, was confirmed by reverse transcription–quantitative PCR (RT–qPCR) (Fig. 1d). Immunoblot analyses confirmed reduced protein levels of ABCG5 and ABCG8 from the ileal epithelium of infected mice (72 h and 96 h p.i.) compared to control animals (Fig. 1f). Two LXRs, LXRα (NR1H3) and LXRβ (NR1H2), play key roles in the transcriptional regulation of genes involved in cholesterol homeostasis[23]. Interestingly, the protein level of LXRβ was decreased, while LXRα level remained unchanged in the ileum of infected neonates compared to the control groups (72 h and 96 h p.i.) (Fig. 1f), suggesting repression of the LXR pathway following infection. In contrast, most cholesterol biosynthesis genes were upregulated after *C. parvum* infection (Fig. 1b,c), as validated by RT-qPCR (Fig. 1e). The rate-limiting enzyme in cholesterol biosynthesis is 3-hydroxy-3-methylglutaryl-CoA reductase (HMGCR)[24]. Immunoblot analyses of cytosolic protein extracts confirmed the higher levels of HMGCR protein in the ileum of infected neonates compared to the control groups (Fig. 1f). Furthermore, we found a

significant reduction of free cholesterol in the ileum of infected neonatal mice compared to control mice (Fig. 1h).

Strikingly, the proximal small intestine, which is primarily responsible for nutrient absorption and is not infected with *C. parvum* (Extended Data Fig. 1a,b), also exhibited similar changes in the expression levels of cholesterol homeostasis genes (Fig. 1g and Extended Data Fig. 2e). Notably, RT-qPCR showed an increased expression of NPC1L1 in the proximal small intestine but decreased expression in the ileum (Fig. 1d and Extended Data Fig. 2e). Furthermore, a significant reduction in total cholesterol was detected in the proximal small intestinal epithelium of infected neonates compared to the control groups (Fig. 3g and Extended Data Fig. 6a). Most of the cholesterol absorbed by the intestine is secreted as chylomicrons into the circulation[25]. Expression of genes involved in the chylomicron assembly was significantly reduced in both the proximal small intestine and ileum of infected animals (Extended Data Fig. 2f-h). Consistent with results from previous studies[8,21], the villi length in the infected ileum was significantly shorter (Extended Data Fig. 2j), whereas no such change was observed in the non-directly infected region of the intestine (Extended Data Fig. 2j). Additionally, the small intestine length in infected neonates was shorter compared to control animals (Extended Data Fig. 2i), suggesting a reduction in the absorptive surface area in the intestine. Collectively, these findings indicate that *C. parvum* infection disrupts cholesterol homeostasis in the small intestine.

***C. parvum* infection alters hepatic lipid metabolism**

The liver is the primary organ for cholesterol metabolism, and most lipids in the intestine are absorbed by enterocytes in the small intestine, transported through the lymphatic system into the circulation, then to the liver, and eventually to peripheral tissues[26,27]. Based on this, we hypothesized that intestinal infection by *C. parvum* could impact cholesterol and bile acid metabolism in the liver. To test this, we infected neonatal mice with *C. parvum* oocysts for 3 days, collected liver tissues, and performed RNA-seq (Fig. 2a). Consistent with our hypothesis, *C. parvum* infection caused significant alterations in gene expression profiles in the liver (Extended Data Fig. 3a and Supplementary Table 2). GSEA indicated that the major pathways associated with the altered gene expression profiles are related to immune response regulation (Extended Data Fig. 3a). Gene set variation analysis (GSVA) revealed an overall downregulation of genes involved in lipid metabolism pathways in the liver of infected mice, including these related to cholesterol and bile acid metabolism (Supplementary Table 2). RT-qPCR further validated the reduced levels of most genes involved in lipid metabolism (Extended Data Fig. 3b-f). Immunoblot analyses of APOB100 (Apolipoprotein B100), HMGCR, and HMGCS2 (hydroxymethylglutaryl CoA synthase 2) confirmed reduced protein levels in the infected animals (Extended Data Fig. 3g). The protein levels of hepatic FXR and LXRβ were significantly decreased, whereas LXRα remained unchanged after infection (Fig. 2d). Consistent with this, the mRNA expression of most FXR and LXR target genes was significantly reduced in the liver of infected mice (Fig. 2b,c). Immunoblot of selected canonical target genes of LXRs and FXRs, including *ABCG5*, *ABCG8*, *CYP7A1* and *NR0B2* (*Shp*), confirmed decreased protein levels (Fig. 2d). Accordingly, lipidomics analysis revealed altered lipid profiles in the liver of infected mice (Fig. 2a and Extended Data Fig. 4a,b). There was no significant reduction in total lipids in the liver after 4 days infection compared to the control group (Extended Data Fig. 4d,e). However, reduced amounts of bile acids and cholesterol esters, but not total cholesterol, were detected in the liver of infected mice (Fig. 2e and Extended Data Fig. 4f-h). As an important

169 component of milk, fat provides about 50% of the energy for infants[28]. The main fat component
170 is triacylglycerol (TG), which makes up more than 98% of milk fat[29]. We observed significant
171 reductions in most TGs, diacylglycerols (DG), and free fatty acids (FFA) in the liver after *C.*
172 *parvum* intestinal infection (Fig. 2e and Extended Data Fig. 4i-n). Kyoto Encyclopedia of Genes
173 and Genomes (KEGG) pathway enrichment analysis of the lipidomics results revealed
174 downregulation of lipid metabolic pathways in the liver of infected mice (Extended Data Fig. 4c),
175 consistent with the GSVA results from the RNA-seq (Supplementary Table 2). To further
176 investigate the alterations in bile acids, we performed a comprehensive, quantitative bile acid
177 targeted assay (Fig. 2a), which revealed broad metabolic downregulation in the liver of infected
178 mice (Fig. 2f-h). Taken together, these data suggest that *C. parvum* intestinal infection disturbs
179 cholesterol and bile acid homeostasis in the liver.
180
181 **_C. parvum_ infection decreases bile acid levels in the small intestine and reduces the**
182 **absorption of dietary lipids**
183 Given the significant dysregulation of cholesterol and bile acid homeostasis in the liver
184 following *C. parvum* intestinal infection, particularly the decreased expression of FXR-targeted
185 genes, we next investigated lipid metabolism with a focus on the Bile acid-FXR signaling
186 pathway in the infected intestine. FXR is essential for maintaining whole-body bile acid
187 homeostasis by regulating the expression of target genes involved in both hepatic bile acid
188 synthesis and enterohepatic circulation[18]. The enterohepatic circulation of bile acids and the FXR
189 pathway involve the synthesis of bile acids from cholesterol in the liver and the finely controlled
190 expression of genes for bile acids reabsorption in the intestinal epithelium, as shown in Fig. 3a.
191 GSEA indicates that many genes involved in the bile acid metabolic process in the ileum were
192 significantly reduced in infected mice (Fig. 3b). The reduction of FXR and FXR-targeted genes
193 *Shp* and *Fgf15* suggests a robust suppression of FXR signaling in the small intestine following
194 infection (Fig. 3b-d and Extended Data Fig. 5a). Bile acids generate negative feedback on ileal
195 ASBT transcription through FXR-mediated induction of *Shp*[30]. Notably, despite a substantial
196 increase in its mRNA expression (Fig. 3b,c), ASBT was markedly reduced at the protein level
197 (Fig. 3d), which could substantially impact bile reabsorption in the ileum.
198
199 To address whether dysregulation of liver and intestinal bile acid metabolism affects the bile
200 levels in the small intestine following infection, we infected neonatal mice with *C. parvum*
201 oocysts for 4 days. We then collected small intestine tissues, including the luminal contents, and
202 performed a comprehensive, quantitative bile acid targeted assay. A marked decrease of most
203 intestinal bile acids was observed in the infected mice (Fig. 3h and Extended Data Fig. 6d). In
204 addition, the ileum appears paler, possibly due to a reduction in intestinal bile acids following the
205 infection (Extended Data Fig. 5d). RNA-seq analysis of ileal tissues revealed a global decrease in
206 the expression of genes involved in lipid and vitamin absorption in the infected mice (Extended
207 Data Fig. 5g,h). Imaging of neutral lipids by oil red O (ORO) staining[31] showed a reduction in
208 neutral lipids in the proximal small intestine and ileum following infection (Fig. 3e). Consistent
209 with this, lipidomics analysis demonstrated a significant decrease in total lipids (Fig. 3f),
210 particularly bile acid, cholesterol, phosphatidylcholines (PC), hexosylceramides (HexCer-NS)
211 and Ceramide-NS (Cer-NS) in the proximal small intestinal epithelium of infected neonates (Fig.
212 3g and Extended Data Fig. 6a). However, lipidomics analysis showed no significant alteration in
213 total TG level (Fig. 3g and Extended Data Fig. 6a). Additionally, the proximal small intestinal
214 epithelium and ileum from infected neonates exhibited reduced expression of several genes

involved in fatty acid oxidation, TG catabolism (Extended Data Fig. 5b,c,e,f), and chylomicron assembly (Extended Data Fig. 2f-h). Furthermore, lower levels of L-palmitoylcarnitine were detected in the proximal small intestinal epithelium of *C. parvum* infected neonates (Extended Data Fig. 6c), indicating impaired fatty acid oxidation. These alterations may contribute to the accumulation of TG in the proximal small intestinal epithelium following infection. Linoleic acid is an essential lipid that cannot be synthesized in mammalian cells and is exclusively acquired from the diet[32]. The KEGG pathway enrichment analysis of lipidomics revealed a reduction in linoleic acid metabolism (Extended Data Fig. 6b), further supporting the reduced absorption of dietary lipids in the intestine after *C. parvum* infection.

Bile intervention shows therapeutic potential for intestinal cryptosporidiosis

To assess the impact of reduced bile on the pathogenesis of *C. parvum* infection, we administered whole bile collected from the gallbladders of adult mice to neonates (5 days old) at 24 h after oral gavage of *C. parvum* oocysts, followed by daily administration of bile for an additional 3 days (Fig. 4a). Bile feeding activated intestinal transcription of FXR target genes (Fig. 4c) and surprisingly, greatly reduced the infection burden compared to the animals receiving PBS (Fig. 4b). Our data revealed significant variation in infection burden across different regions, with the highest levels typically observed in the distal ileum (Fig. 4d). Notable reductions in the infected area of the distal ileum and overall reduced infection burden were observed in the intestinal tissues of animals receiving bile, compared to the PBS-treated control group (Fig. 4d). Additionally, replenishing bile restored the ileal expression of genes involved in cholesterol homeostasis in the infected mice (Extended Data Fig. 7a,b). Furthermore, human intestinal epithelial HCT-8 cells were first exposed to *C. parvum* infection for 4 h (a time frame for parasite attachment and invasion)[33], after which free-parasites were removed after washing. Cell cultures were then exposed to various concentrations of bile or PBS for an additional 20 h, followed by measurement of infection burden. A substantial reduction in infection burden was observed in cells treated with higher concentrations of bile (0.5% and 1%) compared to lower bile concentrations (0.2%, 0.25% and 0.33%) (Fig. 4e,f). Interestingly, an increased infection burden was noted in cultures treated with lower concentrations of bile compared to the PBS group (Fig. 4e,f). Primary 2D intestinal epithelial monolayers derived from mice for *C. parvum ex vivo* infection further confirmed this phenomenon (Extended Data Fig. 7e). Data from previous reports show that bile salt sodium taurocholate enhances excystation and the entry of *Cryptosporidium* into host cells[34]. Consistent with this, we observed an overall increase in infection burden when HCT-8 cells were exposed to *C. parvum* oocysts in the presence of various bile concentrations (from 0.07%-2% bile acids as tested) during the 4 h parasite attachment and invasion time frame (Extended Data Fig. 7d). HCT-8 cells exposed to different concentrations of bile, with or without *C. parvum* infection, showed no significant reduction in cell viability (Extended Data Fig. 8a-d). To further assess the therapeutic potential of bile for cryptosporidiosis. We orally inoculated neonatal mice with excessive dose of *C. parvum* (2×10^6 oocysts per animal). At 24 h after *C. parvum* infection, mice were fed different doses of whole bile collected from the gallbladders of adult mice (0.5, 1.5, and 3 μl of bile per animal, diluted with PBS), followed by daily for another 3 days (Fig. 5a). Resultant data further support a role for bile in reducing infection and increasing lipid uptake following *C. parvum* infection (Fig. 5b-f and Extended Data Fig. 7c). Specifically, feeding 1.5 and 3 μl of bile per day for 4 days activated intestinal transcription of FXR target genes (Fig. 5e) and greatly decreased the infection burden compared to the animals receiving PBS (Fig. 5d,f and Extended Data Fig. 7c),

while feeding 0.5 μl of bile per day did not cause significant changes (Fig. 5b,c). Notably, in the presence of excessive dose of *C. parvum* inoculation, treatment with 3 μl of bile per day for 4 days greatly reduced the infected area from distal ileum in mice, which was negatively correlated with the area and extent of intestinal lipid absorption (Fig. 5f and Extended Data Fig. 7c).

Bile acid-FXR signaling pathway is involved in the regulation of intestinal epithelium turnover in response to *C. parvum* infection

To monitor the cell proliferation and epithelial turnover in the intestine following infection, we examined the incorporation of ethynyl-2'-deoxyuridine (EdU) and tracked the migration of EdU-labeled cells at 4 and 48 h after EdU pulse labeling (Fig. 6a). To explore the potential effects of bile, we gavaged infected and uninfected mice with the whole bile collected from the gallbladders of adult mice (Fig. 6a). As shown in Fig. 6e and Extended Data Fig. 9a, there was a significant increase in the number of EdU-positive proliferating cells in the crypt regions of infected mice at 4 h. These proliferative cells also migrated much higher along the villus compared to their control counterparts at 48 h p.i. (Fig. 6g,j). Interestingly, quantification showed an appreciable decrease in EdU-positive proliferating and migrating cells in infected mice treated with bile compared to those treated with PBS (Fig. 6e,g,j and Extended Data Fig. 9a). Notably, we found that the dysregulation of cell proliferation and migration induced by infection, as well as the effects of bile supplement, were not limited to the ileum but extended to the entire small intestine and even the colon (Fig. 6c-j and Extended Data Fig. 9a).

There was a significant increase in the transcription levels of FXR target genes in infected mice treated with bile compared to those treated with PBS (Fig. 4c and Fig. 5e). We then examined whether activation of FXR pathway could attenuate crypt hyperproliferation and cell migration *in vivo*. We administrated mice with Fexaramine (FexD) (Fig. 7a), which has previously been shown to activate FXR pathways *in vivo* [35]. Quantification showed a significant decrease in EdU-positive proliferating and migrating cells (jejunum and ileum) in uninfected mice treated with FexD compared to those treated with vehicle control (Fig. 7b-g). This was consistent with previous literature that the activation of FXR pathway inversely correlates with epithelial proliferation, colorectal cancer progression and malignancy [36–38]. Interestingly, EdU-labeling analysis demonstrated an even more pronounced decrease in EdU-positive proliferating and migrating cells between infected mice treated with FexD and vehicles, compared to those uninfected mice treated with FexD and vehicles (Fig. 7b-g). Notably, FXR activation significantly increased the infection burden (Fig. 7h,i), further emphasizing the critical role of FXR signaling in maintaining crypt-villus homeostasis during *Cryptosporidium* infection. Importantly, this effect appears to be independent of the infection burden. RT-PCR indicated that bile treatment for 6 h can activate intestinal transcription of FXR target genes in uninfected mice (Fig. 6b). However, in contrast to *C. parvum* infected mice, no significant differences were observed in uninfected mice treated with bile and PBS (Fig. 6c-j and Extended Data Fig. 9a). The negative feedback of bile acid-FXR axis might restrain the constant activation of FXR pathway in uninfected mice [18]. Overall, these data suggest that the Bile acid-FXR signaling pathway is involved in regulating cell proliferation and migration of the intestinal epithelium following *C. parvum* infection.

Discussion

306 The preferred site of *Cryptosporidium* infection is the ileum, where sporozoites penetrate
307 individual epithelial cells (mainly enterocytes). After cell entry, they form a unique apical
308 localization (intracellular but extra-cytoplasmic), preventing the infection from further spreading
309 to deeper epithelial tissues or entering the circulation and infecting other organs[39,40]. The
310 significant alterations in gene expression profiles and metabolic processes observed in the liver,
311 and proximal small intestine - regions where no parasites were detected - suggest that the
312 pathological changes extend beyond the directly infected ileum. From a pathological perspective,
313 the metabolic dysregulation observed beyond the ileum may play an important role in the growth
314 stunting and malnutrition seen in young children following cryptosporidial infection.
315
316 The correlation between lipid and bile acid metabolic dysregulation observed in the liver and
317 intestine from infected mice provides further evidence of the role of the gut-liver axis in the
318 pathogenesis of various enteritis. Given the preferred infection site of *Cryptosporidium* in the
319 ileum, where over 95% of the bile acids are reabsorbed[13], it maybe pathologically significant that
320 the expression of ASBT is downregulated at the protein level in the infected ileum. This
321 downregulation could reduce bile acid reabsorption, contributing to the decreased bile acid levels
322 in the enterohepatic circulation. Depletion of intestinal cholesterol may also contribute to the
323 decreased bile acid pool, as ASBT function depends on the cholesterol content of lipid raft
324 domains in the plasma membrane[41]. Moreover, the decreased absorptive surface area in the
325 intestine, due to the loss of microvilli and shorten of villus height and intestinal length following
326 *Cryptosporidium* infection, could decrease the brush border apical surface. Surprisingly, the
327 reduction of the bile acid pool and the downregulation of the FXR pathway in the enterohepatic
328 circulation following *C. parvum* infection did not lead to an increase in hepatic bile synthesis as
329 compensation. Instead, there was an overall decrease in bile acid metabolism in the liver. Hepatic
330 bile synthesis generally accounts for only a small fraction of the bile acid pool, as over 95% bile
331 acids are conserved through intestinal reabsorption in the enterohepatic circulation[42].
332
333 While most bile acids are transported back into the liver via enterohepatic circulation, a small
334 fraction of this pool (roughly 5%) escapes reabsorption in the ileum and is further converted into
335 secondary bile acids in the colon by the gut microbiota[13]. Previous studies have demonstrated
336 controversial effects of several bile acids on *Cryptosporidium* infection. Three secondary bile
337 acids (deoxycholate, deoxycholic acid, and lithocholic acid) have been reported to impair
338 *Cryptosporidium* growth *in vitro*[43]. The bile salt sodium taurocholate enhances microneme
339 secretion and increases the entry of *Cryptosporidium* into host cells[34]. Our studies indicate that
340 total bile collected from the gallbladder of adult mice can enhance the entry of *Cryptosporidium*
341 into cultured host epithelial cells. However, adequate supplementation with collected bile
342 significantly reduces the infection burden both *in vivo* and *in vitro*. Additionally, treatment with
343 bile collected from the gallbladder of adult mice or the FXR agonist FexD ameliorates
344 dysregulated cell proliferation and migration in the intestine, including both the directly infected
345 ileum region and the non-infected regions. Several previous studies have suggested a potential
346 association between cryptosporidiosis and the presence of digestive neoplasia[44]. It remains to be
347 determined whether there is an association between Bile acid-FXR pathway and the development
348 of digestive neoplasia following *Cryptosporidium* infection.
349
350 Although obvious disturbances in cholesterol and bile homeostasis in the gut-liver axis were
351 observed following *Cryptosporidium* infection, the underlying mechanisms driving these

352 metabolic disturbances remain unclear. In addition to reduced bile acid pool and subsequent lipid
353 malabsorption, the general inflammatory responses triggered by infection as previously
354 reported[45] may play a role. If so, it would be interesting to explore whether these findings are
355 applicable to infection caused by other gastrointestinal pathogens. In the intestinal epithelium,
356 these disturbances may also reflect the immature state of the epithelial cell population during
357 infection. Previous studies have shown that infection with this parasite accelerates ileal epithelial
358 development, resulting in an epithelium dominated by immature cells[46]. The outgrowth of
359 immature epithelial cells, which are actively progressing through the cell cycle and not yet fully
360 differentiated, may contribute to lipid malabsorption. Biliary infection by *Cryptosporidium*, as
361 reported in AIDS patients and other weakened immune systems[11], may have additional effects on
362 cholesterol and bile homeostasis. Additionally, bile acids have been shown to drive the
363 maturation of the newborn's gut microbiota[47]. Gut microbiome development is closely linked to
364 the overall development of the child, with changes in its composition and maturity potentially
365 affecting immune functions, intestinal development, neurodevelopment, nutritional energy
366 harvest, growth, and weight gain[48]. The composition and diversity of the gut microbiome during
367 early development play a crucial role in the incidence and severity of *Cryptosporidium*
368 infection[49–51]. Whether bile treatment influences the maturation of the gut microbiota and, in turn,
369 improves long-term deficits in growth, weight gain, and cognitive development following
370 *Cryptosporidium* infection warrants further exploration.
371

372 # Methods

373 **Ethics statement**

374 All research studies involving the use of animals were reviewed and approved by the
375 Institutional Animal Care and Use Committee (IACUC) of Rush University at Chicago, Illinois,
376 and were carried out in strict accordance with the recommendations in the Guide for the Care and
377 Use of Laboratory Animals.
378

379 ***C. parvum* and Cell lines**

380 *C. parvum* oocysts of the Iowa strain were obtained from a commercial source (Bunch Grass
381 Farm, Deary, ID). HCT-8 cells were purchased from ATCC (Manassas, Virginia). The culture
382 media were supplied with 10% fetal bovine serum (FBS) (Ambion, Austin, Texas) and
383 antibiotics (100 IU/ml of penicillin and 100 µg/ml of streptomycin).
384

385 **Histology of intestinal tissue**

386 Neonatal mice were killed and small intestine was dissected. Given the stand 'swiss-roll' was not
387 feasible with the unfixed small intestines of neonatal mice due to their fragility. We collected
388 fresh tissue, gently rolled it into a spiral shape, and embedded it in OCT compound for
389 subsequent analysis. Slides were evaluated in a blinded fashion for measurements of parasite
390 burden, and Oil red staining (see Fig. 5f and Extended Data Fig. 7c). A section four centimeters
391 from the stomach of neonatal mice as the proximal small intestine (jejunum), and the distal small
392 intestine four centimeters from the cecum as the ileum for subsequent analysis (RT-qPCR,
393 Immunoblotting, Immunohistochemistry, and Oil red staining).
394

395 **Bile collection**

396 Gall bladders were removed from healthy adult C57BL/6 mice after 24 hours of fasting,
397 punctured with forceps to collect bile, and stored at -80°C until processing.

398
399 ***In vitro C. parvum* infection experiments**
400 Models of intestinal cryptosporidiosis using cultured cell lines were employed as previously
401 described[52]. For *C. parvum* infection burden experiments, infection was done in serum-free
402 culture medium for 4 h with a 1:4 ratio of *C. parvum* oocysts to HCT-8 cells. The culture
403 medium was changed to remove free parasites. The medium was supplemented with mouse bile
404 at concentrations of 0.2%, 0.25%, 0.33%, 0.5% and 1% (collected by gall bladder puncture from
405 healthy adult C57BL/6 mice) and cultured for an additional 20 h (a total 24 h p.i.), followed by
406 infection burden measurement. Infection burden was quantified by measuring levels of *C.*
407 *parvum* 18S gene (*cp18S*)[53]. Immunofluorescent staining of *C. parvum* was carried out using
408 rabbit antiserum against *C. parvum* membrane proteins as previously described[54,55]. For *C.*
409 *parvum* invasion experiments, HCT-8 cells were incubated with *C. parvum* oocysts (1:4 ratio of
410 oocysts to cells) in the presence of various concentrations of bile (0.07%, 0.2%, 1%, and 2%) or
411 PBS for 4 h, followed by RT-qPCR of *cp18S*.
412
413 ***In vivo C. parvum* infection experiments**
414 A well-established infection model of cryptosporidiosis in neonatal mice was used for *in vivo*
415 experiments[56,57]. Neonatal mice (5 days old) were orally inoculated with *C. parvum* (10^6 oocysts
416 per animal). Mice receiving PBS by oral gavage were used as control. At 72 and 96 h after *C.*
417 *parvum* oocysts or PBS administration, the animals were sacrificed, and intestine and liver
418 tissues were collected for biochemical analyses. For *C. parvum* infection burden experiments,
419 neonatal mice (5 days old) were orally inoculated with *C. parvum* (at a lower dose of 10^5 oocysts
420 per animal). At 24 h after *C. parvum* infection, the animals were fed with PBS-diluted bile (0.5,
421 1.5, 3, and 3,5 µl bile per animal, diluted in PBS to a total volume of 7 µl) and PBS (7µl per
422 animal), followed by daily for 4 days. The animals were sacrificed, and intestine tissues were
423 collected for biochemical analyses.
424
425 **RT-qPCR**
426 Total RNA was isolated using TRIzol™ Reagent (Thermo Fisher Scientific, catalogue no.
427 15596018), and genomic DNA was removed using the DNA-free™ DNA Removal Kit (Thermo
428 Fisher Scientific, catalogue no. AM1906). The reverse-transcription reaction was performed on
429 2 µg total RNA with M-MLV Reverse Transcriptase (Thermo Fisher Scientific, catalogue no.
430 28025013). Quantitative PCR assays were conducted using Bio-Rad CFX Manager v3.1 using
431 the iTaq™ Universal SYBR® Green Supermix (Bio-rad, Hercules, CA, USA, catalogue no.
432 1725124). RNA expression levels were calculated using the ΔΔCt method.
433
434 **RNA-Seq and bioinformatic analysis**
435 Total RNAs isolated with Rneasy Mini Kit (QIAGEN, catalogue no. 74104). Three biological
436 replicates (all mice from the same litter) were performed for each condition. The samples were
437 analyzed by BGI Americas Corporation (Cambridge, MA) using the DNBSEQ™ sequencing
438 technology platform, as previously reported[21]. Differential expression analysis and statistical
439 significance were assessed using DESeq in R with a standard negative binomial fit for the
440 aligned counts data and are described relative to the indicated control (Table S1 and S2). Gene
441 set enrichment analysis (GSEA) was performed using the R package "clusterProfiler"[58] with
442 gene sets from the MsigDB database (http://www.gsea-msigdb.org/gsea/index.jsp)[59]. Gene set
443 variation analysis (GSVA) was conducted with a significance threshold of $p < 0.05$ to explore

correlated pathways, using gene sets from the MsigDB database[60]. Bioinformatic analysis was carried out and results were employed as we previously reported[21,61].

Immunoblotting

Membrane and cytosolic protein extracts were isolated from frozen mouse liver or small intestine (30 mg) using the Mem-PER Plus Membrane Protein Extraction Kit (Thermo Fisher Scientific, Catalog no. 89842). Membrane and cytosolic fractions were separated by SDS-PAGE and transferred to a nitrocellulose membrane. Images were captured using the ChemiDoc MP Imaging System (Bio-Rad, Catalog no. 12003154). The following primary and secondary antibodies were used: anti-β Tubulin (Santa Cruz, catalogue no. sc-5274, 1:1000), anti-GAPDH (Santa Cruz, catalogue no. sc-32233, 1:1000), anti-ABCG5 (Thermo Fisher Scientific, catalogue no. BS-5013R, 1:1000), anti-ABCG8 (Novus Biologicals, catalogue no. 1B10A5, 1:1000), anti-SLC10A2 (Abcam, catalogue no. ab203205, 1:1000), anti-FGF15 (Santa Cruz, catalogue no. sc-514647, 1:1000), anti-NR1H4 (Proteintech, catalogue no. 25055-1-AP, 1:3000), anti-NR1H3 (Proteintech, catalogue no. 14351-1-AP, 1:5000), anti-NR1H2 (Proteintech, catalogue no. 60345-1-Ig, 1:1000), anti-Na+/K+-ATPase (Abclonal, catalogue no. A12405, 1:2000), anti-HMGCR (Abclonal, catalogue no. A1633, 1:2000), anti-CYP7A1 (Abclonal, catalogue no. A10615, 1:1000), anti-NR0B2 (Abclonal, catalogue no. A1836, 1:500), anti-HMGCS2 (Abclonal, catalogue no. A19232, 1:2000), anti-rabbit B700 (Bio-Rad, catalogue no. 12004161, 1:2500), anti-mouse B700 (Bio-Rad, catalogue no. 12004158, 1:2500), anti-rabbit B520 (Bio-Rad, catalogue no. 12005869, 1:2500), anti-mouse B520 (Bio-Rad, catalogue no. 12005866, 1:2500), anti-GAPDH hFAB™ Rhodamine (Bio-Rad, catalogue no. 12004167, 1:2500), anti-Tubulin hFAB™ Rhodamine (Bio-Rad, catalogue no. 12004165, 1:2500).

Immunohistochemistry

For tissue staining, frozen sections (8 μm) were fixed in 4% PFA in PBS for 15 min, then washed twice with PBS. The sections were permeabilized by adding 0.5% Triton X-100 (Bio-rad, catalogue no. 1610407) in PBS for 20 min, followed by removal of the permeabilization buffer and two PBS washes. Sections were then blocked for 30 min in 10% normal donkey serum, 0.1% Triton X-100, 0.01% sodium azide in PBS before incubation with the primary antibody for 2 h at room temperature or overnight at 4 °C. Slides were washed three times with PBS and incubated in block solution containing secondary antibody for 30 min at room temperature. After antibody incubation, sections were washed three times with PBS (5 min per wash) and mounted with Antifade Mounting Medium with DAPI (Vector, catalogue no. H-1200). Images were captured using a Keyence BZ-X810 microscope. For cell staining, HCT-8 cells were fixed in 4% PFA in PBS for 15 min and washed twice with PBS. Fixed cells were permeabilized with 0.1% Triton X-100 in PBS for 5 min and washed three times with PBS. Cells were blocked for 30 min in 10% normal donkey serum, 0.1% Triton X-100, 0.01% sodium azide in PBS, followed by incubation with primary antibody for 1 h at room temperature. Cells were then washed three times with PBS and incubated in block solution containing secondary antibody for 30 min at room temperature. Following antibody incubation, cells were washed three times with PBS (5 min per wash) and mounted with Antifade Mounting Medium with DAPI (Vector, catalogue no. H-1200). Images were taken using a Keyence BZ-X810 microscope. Immunofluorescent staining of *C. parvum* was carried out using rabbit antiserum against *C. parvum* membrane proteins as previously described[54,55]. Other antibodies used for immunofluorescent staining include anti-Ki67 antibody (Cell Signaling Technology, catalogue no. 9129, 1:200), anti-ABCA1 antibody (Thermo Fisher Scientific, catalogue no. PA1-16789, 1:200), goat-anti-bovine Alexa fluor 488 (Jackson Immuno

491 Research, catalogue no. 101-545- 003, 1:250), goat-anti-bovine Alexa fluor 594 (Jackson
492 Immuno Research, catalogue no. 101-585- 003, 1:250), donkey-anti-rabbit Alexa fluor 488
493 (Jackson Immuno Research, catalogue no. 711-545-152, 1:500), donkey-anti-rabbit Rhodamine
494 Red (Jackson Immuno Research, catalogue no. 711-295-152, 1:500).
495
496 **Oil red staining**
497 Lipid vesicle storage in tissue was assessed with Oil Red O staining, following the
498 manufacturer's protocol (Abcam, catalogue no. ab150678). Images were captured using a
499 Keyence BZ-X810 microscope.
500
501 **Cell viability**
502 Cell viability was assessed using a Neutral Red Assay Kit, following the manufacturer's
503 instructions (Abcam, catalogue no. ab234039). The absorbance of each well at 540 nm was
504 measured using a microplate reader (SpectraMax iD3, Molecular Devices, USA) to evaluate the
505 cell viability.
506
507 **Bile Acid Targeted Metabolomics Assay**
508 Metabolites were extracted from the livers and small intestines of control and *C. parvum*-infected
509 neonatal mice, with three biological replicates for each condition. The samples were analyzed by
510 Metware Biotechnology Inc (Metware). Metabolomics profiling was employed as previously
511 described[62].
512
513 **Quantitative Lipidomics**
514 Metabolites were extracted from the livers and proximal intestinal epithelium of control and *C.*
515 *parvum* infected neonatal mice, with four biological replicates for each condition. The samples
516 were analyzed by Metware Biotechnology Inc (Metware). Metabolomics profiling was employed
517 as previously described[63].
518
519 **Cholesterol assay**
520 Cholesterol Quantification Assay Kit (Sigma-Aldrich, CS0005) was used to measure the
521 cholesterol concentration of samples. We sampled the distal small intestine four centimeters
522 from the cecum of neonatal mice and collected epithelial cells. Briefly, 46 µL Assay Buffer, 2 µL
523 Probe, 2 µL Enzyme Mix, and 50 µL sample were mixed and incubated at 37 °C for 30 min in
524 each well. A calibration curve was established for every measurement with standard samples
525 with 0–5 µg cholesterol. All samples were diluted to the range of the calibration curve with the
526 Assay Buffer. Absorbance at 570 nm was measured and compared to the standards on the same
527 plate to determine total cholesterol.
528
529 ***In vivo* EdU assay**
530 Neonatal mice (5 days old) were orally inoculated with *C. parvum* (10^5 oocysts per animal).
531 Mice receiving PBS by oral gavage were used as control. For bile treatment, 24 h after *C.*
532 *parvum* oocysts or PBS administration, control mice were treated with PBS, *C. parvum*-infected
533 mice were fed PBS-diluted bile (7µl per animal,1:1 ratio of bile to PBS) or PBS only (7µl per
534 animal), followed by daily treatments for 3 days. Mice were i.p. injected with EdU and sacrificed
535 4 h post injection. In another group, mice were i.p. injected with EdU, treated with PBS-diluted
536 bile or PBS for an additional 2 days, and sacrificed 48 h post injection. For FXR agonists
537 fexaramine D (FexD) treatment, 24 h after *C. parvum* oocysts or PBS administration, control

538 mice were i.p. injected with vehicle, and *C. parvum*-infected mice were i.p. injected with vehicle
539 with or without 100 mg/kg of FexD, followed by daily treatments for 3 days. Mice were i.p.
540 injected with EdU and sacrificed 4 h post injection, or were i.p. injected with EdU, treated with
541 vehicle with or without FexD for an additional 2 days and sacrificed 48 h post injection. Intestine
542 tissues were frozen in OCT and cryosectioned (10 μm). EdU staining was performed using the
543 Click-iT EdU imaging kit (Thermofisher cat# C10337) according to the manufacturer's protocol.
544 To evaluate the proliferation and migration of EdU-labeled cells, we calculated the average
545 values across all villi/crypts within the same group as previously reported[64].
546
547 **Bioinformatic analysis of metabolomics**
548 Multivariate analysis of Variable Importance in Projection (VIP) from OPLS-DA modeling
549 (MetaboAnalystR, v.1.0.1) was used to preliminarily select differential metabolites from
550 different samples. For two-group analysis, differential metabolites were determined by VIP
551 (VIP > 1) and P-value (P-value < 0.05, Student's t test). The data were log-transformed (log_2)
552 and mean-centered prior to OPLS-DA. To avoid overfitting, a permutation test (200
553 permutations) was performed. For KEGG annotation and enrichment analysis, identified lipids
554 were annotated using the KEGG Compound database (http://www.kegg.jp/kegg/compound/).
555 Annotated lipids were then mapped to the KEGG Pathway database
556 (http://www.kegg.jp/kegg/pathway.html). Pathways with significantly regulated lipids were
557 further analyzed using the MSEA (lipid sets enrichment analysis), with significance determined
558 by the hypergeometric test's p-values.
559
560 **Statistical analysis**
561 For all quantitative analyses, a minimum of three biological replicates were included. Statistical
562 tests were selected based on the assumption that sample data are from a population following a
563 probability distribution with a fixed set of parameters. Student's t-tests were used to assess the
564 statistical significance of differences between two groups. One-way AVOVA was used for
565 multiple comparison tests. The following values were considered statistically significant:
566 *P < 0.05, **P < 0.01, ***P < 0.001, ****P < 0.0001. Calculations were performed using the
567 GraphPad Prism 10 software package. Data are presented as mean ± the standard error of the
568 mean.
569
570 **Data availability**
571 The RNA-seq data generated in this study have been deposited into NCBI's Gene Expression
572 Omnibus (GEO) and are accessible through GEO series accession number GSE234579 and
573 GSE272799. The metabolomics analysis data are presented in Table S3-S6. Uncropped images
574 of immunoblots presented in the figures are included in Supplementary Figure 1. Source data are
575 available with this paper.
576
577 ## Figure legends
578 **Fig.1 | *C. parvum* infection disrupts cholesterol homeostasis in the small intestine.**
579 **a,** Schematic diagram summarizing the molecular mechanism of cholesterol transport.
580 **b,** Changes in cholesterol homeostasis-related gene expression upon *C. parvum* infection (72 h
581 p.i.). The enrichment of cholesterol biosynthesis and efflux gene sets is shown at the bottom. The
582 upregulated and downregulated genes (log2FC > 0.5, adj. p < 0.05) are indicated by the light
583 red– and light blue–shaded rectangles underlaid on plot, respectively.

584 **c,** Schematic of the cholesterol biosynthesis pathway, where genes are represented in blue.
585 **d, e,** Relative amounts of mRNAs analyzed by RT–qPCR. Gene expression was presented as fold
586 change to uninfected control.
587 **f, g,** Immunoblotting analysis of ileum and proximal intestinal epithelial cells (IECs) in neonates
588 with and without *C. parvum* infection (72 h and 96 h p.i.). GAPDH and TUBULIN were used as
589 loading control of cytosolic protein.
590 **h,** Quantification of free cholesterol in ileum of control and infected mice (96 h p.i.).
591 Each symbol represents one mouse, all from the same litter. Statistical analysis: unpaired t test
592 for (d, e). Data are expressed as mean ± SEM, and representative of at least two independent
593 experiments, n = 3–5 per group. *P < 0.05, **P < 0.01, ***P < 0.001, ****P < 0.0001. For gel
594 source data, see Supplementary Figure 1.
595
596 **Fig.2 | *C. parvum* infection alters hepatic lipid metabolism.**
597 **a,** Experiment schematics: Neonatal mice (5 days old) were orally inoculated with *C. parvum*
598 oocysts (10^6 oocysts per animal), and liver tissues were collected for deep sequencing (72 h p.i.)
599 and metabolomics (96 h p.i.).
600 **b,** Clustered heatmap of normalized gene counts of LXR and FXR target genes expression in the
601 liver of *C. parvum* infected neonatal mice versus control mice (72 h p.i.).
602 **c,** RT-qPCR analysis confirming hepatic mRNA expression of LXR and FXR target genes in
603 neonates with and without *C. parvum* infection at 72 h p.i.
604 **d,** Immunoblotting analysis of liver samples in control and *C. parvum* infected neonatal mice (72
605 h p.i.). GAPDH and TUBULIN were used as loading control of cytosolic protein.
606 **e,** Scatter plot showing the change of hepatic lipids between control or *C. parvum* infected mice
607 in different subclasses (96 h p.i.). Lipid with VIP ≥ 1 represents significant difference.
608 **f,** Heatmap of differential hepatic bile acids expression in control versus *C. parvum* infected mice
609 (96 h p.i.).
610 **g,** The total quantification of all bile acids in liver between control and *C. parvum* infected
611 neonatal mice from (f).
612 **h,** Structures of cholesterol and bile acids. Bile acids are synthesized from cholesterol and can be
613 amidated by taurine (or glycine).
614 Each symbol represents one mouse, all from the same litter. Statistical analysis: unpaired t test
615 for (c, g). Data are expressed as mean ± SEM, and representative of at least two independent
616 experiments, n = 3–5 per group. *P < 0.05, **P < 0.01, ***P < 0.001, ****P < 0.0001. For gel
617 source data, see Supplementary Figure 1.
618
619 **Fig.3 | *C. parvum* infection decreases bile acid levels in the small intestine and reduces the**
620 **absorption of dietary lipids.**
621 **a,** Schematic overview of the enterohepatic circulation of bile acids and the FXR pathway.
622 **b,** Differential gene expression analysis upon *C. parvum* infected neonatal mice (72 h p.i.). The
623 enrichment of bile acid metabolic gene set is shown in blue and the distribution of Shp and
624 ASBT is shown in orange.
625 **c,** RT-qPCR analysis confirming ileum mRNA expression of FXR, Fgf15, Shp and ASBT from
626 infected neonates (72 h p.i.).
627 **d,** Immunoblotting analysis of ileum samples in control and *C. parvum* infected neonatal mice
628 (72 h and 96 h p.i.). GAPDH and TUBULIN were used as loading control of cytosolic protein,
629 Na+/K+ ATPase was used as loading control of membrane protein.

e, Oil Red O stains of the proximal small intestine and ileum section in neonates with and without *C. parvum* infection (96 h p.i.).
f, The total quantification of all lipids in proximal IECs between control and *C. parvum* infected neonatal mice.
g, Scatter plot showing the change of proximal IECs lipids between control or *C. parvum* infected mice in different subclasses. Neonatal mice (5 days old) were orally inoculated with *C. parvum* oocysts (10^6 oocysts per animal) and proximal IECs were collected (96 h p.i.) for lipidomics analysis. Lipid with VIP ≥ 1 represents significant difference.
h, Heatmap of differential intestinal bile acids expression in control versus *C. parvum* infected mice. Neonatal mice (5 days old) were orally inoculated with *C. parvum* oocysts (10^6 oocysts per animal) and small intestine was collected (96 h p.i.) for bile acid targeted assay.
Each symbol represents one mouse, all from the same litter. Statistical analysis: unpaired t test for (c, f). Data are expressed as mean ± SEM, and representative of at least two independent experiments, n = 3–4 per group. *P < 0.05, **P < 0.01, ***P < 0.001, ****P < 0.0001. For gel source data, see Supplementary Figure 1.

Fig.4 | Bile intervention promotes intestinal anti-*C. parvum* defense.
a, Experiment schematics: Neonatal mice (5 days old) were orally administered 1×10^5 *C. parvum* oocysts; PBS and bile were given at 24 h p.i. followed by daily for 4 days, respectively; Intestinal tissues were collected, and the mRNA levels of infection burden (b) and FXR target genes (c) were measured by RT-qPCR.
d, Immunofluorescent staining of *C. parvum* from (a). A higher magnification of the boxed region to visualize the infection burden of *C. parvum* from different portions of ileum is shown (d). Blue: DAPI, red: Ki67, green: *C. parvum*. Bars, 100 μm.
e, Effects of bile on *C. parvum* infection of cultured HCT-8 cells. Cells were incubated with oocysts for 4 h first, subsequently exposed to different concentrations of bile or PBS for another 20 h, followed by immunofluorescence staining of *C. parvum*. Blue: DAPI (nuclei), red: *C. parvum*. Bars, 100 μm.
f, Effects of bile on *C. parvum* infection of cultured HCT-8 cells. Cells were incubated with oocysts for 4 h first, subsequently exposed to different concentration of bile or PBS for another 20 h, followed by RT-qPCR of *cp18S* (*p<0.05 vs. PBS, ^ p<0.05 vs. 0.2% bile, #p<0.05 vs. 0.25% bile, + p<0.05 vs. 0.33% bile).
Each symbol represents one mouse, all from the same litter. Statistical analysis: unpaired t test for (b, c), one-way analysis of variance (ANOVA) with Tukey tests was used for correction of multiple comparisons in f. Data are expressed as mean ± SEM, and representative of at least two independent experiments, n = 4 per group. *P < 0.05, **P < 0.01, ***P < 0.001, ****P < 0.0001.

Fig.5 | Effects of different doses of bile treatment on *C. parvum* infection *in vivo*.
a, Experiment schematics: Neonatal mice (5 days old) were orally administered 2×10^6 *C. parvum* oocysts; PBS and bile were given at 24 h p.i. followed by daily for 4 days, respectively; Intestinal tissues were collected, and the mRNA levels of infection burden (b, d) and FXR target genes (c, e) were measured by RT-qPCR.
f, Immunofluorescent and Oil Red O staining of the distal small intestine sections from (a). A higher magnification of the boxed region (orange) to visualize the background staining; A higher magnification of the boxed region (red) to visualize the *C. parvum* staining; Red arrow indicates *C. parvum* staining. Blue: DAPI, red: Ki67, green: *C. parvum*. Statistical analysis: unpaired t test

676 for (b-e). Data are expressed as mean ± SEM, and representative of at least two independent
677 experiments, n = 4-5 per group. *P < 0.05, **P < 0.01, ***P < 0.001, ****P < 0.0001.
678
679 **Fig.6 | Bile acid treatment attenuates the dysregulated homeostasis in the intestinal**
680 **epithelium following *C. parvum* infection.**
681 **a,** Experiment schematics: Neonatal mice (5 days old) were orally administered 1×10^5 *C. parvum*
682 oocysts; PBS or bile was given at 24 h p.i. followed by daily for 3 days; Mice were i.p. injected
683 with EdU and sacrificed at 4 h post injection; Mice were i.p. injected with EdU, treated with PBS
684 or bile for another 2 days and sacrificed at 48 h post injection.
685 **b,** RT-qPCR analysis confirming mRNA expression of FXR, Shp, and Fgf15 in the small
686 intestine of uninfected neonates after bile treatment.
687 **c-f**, Quantification of EdU staining of proliferating cells in crypts at 4 h post injection (>50
688 crypts per mouse, 3 mice/group).
689 **g,** Representative images of Ki67, EdU staining of proliferating cells at 48 h post injection. Blue:
690 DAPI (nuclei), red: Ki67, green: EdU. Bars, 100 µm.
691 **h-j,** Quantification of cell migration length along the crypt-villus axis at 48 h post injection.
692 Quantification of cell migration length by measuring the distance from the crypt base to the
693 highest labelled cell in the villus (>30 villus per mouse, 3 mice/group).
694 Statistical analysis: unpaired t test for (b); One-way analysis of variance (ANOVA) with Tukey
695 tests was used for correction of multiple comparisons in c-f, h-j, and representative of at least
696 two independent experiments, n = 3 per group. *P < 0.05, **P < 0.01, ***P < 0.001, ****P <
697 0.0001.
698
699 **Fig.7 | FXR activation attenuates the dysregulated homeostasis in the intestinal epithelium**
700 **following *C. parvum* infection.**
701 **a,** Experiment schematics: Neonatal mice (5 days old) were orally administered 1×10^5 *C. parvum*
702 oocysts; FexD or vehicle were given at 24 h p.i., followed by daily for 3 days; Mice were i.p.
703 injected with EdU and sacrificed at 4 h post injection; Mice were i.p. injected with EdU, treated
704 with FexD or vehicle for another 2 days and sacrificed at 48 h post injection.
705 **b,** Representative images of Ki67, EdU staining of proliferating cells in crypts at 4 h post
706 injection. Blue: DAPI (nuclei), red: Ki67, green: EdU. Bars, 50 µm.
707 **c-e,** Quantification of cell migration length along the crypt-villus axis at 48 h post injection.
708 Quantification of cell migration length by measuring the distance from the crypt base to the
709 highest labelled cell in the villus (>20 villus per mouse, 3 mice/group).
710 **f,** Quantification of EdU staining of proliferating cells in crypts at 4 h (b) post injection (>50
711 crypts per mouse, 3 mice/group).
712 **g,** Representative images of Ki67, EdU staining of proliferating cells at 48 h post injection. Blue:
713 DAPI (nuclei), red: Ki67, green: EdU. Bars, 100 µm.
714 **h, i,** Neonatal mice (5 days old) were orally administered 1×10^5 *C. parvum* oocysts; FexD or
715 vehicle was given at 24 h p.i., followed by daily for 3 days; Ileum tissues were collected, and
716 the mRNA levels of FXR target genes (h) and infection burden (i) were measured by RT-
717 qPCR.
718 Statistical analysis: unpaired t test for (h, i); One-way analysis of variance (ANOVA) with Tukey
719 tests was used for correction of multiple comparisons in c-f, and representative of at least two
720 independent experiments, n = 3 per group. *P < 0.05, **P < 0.01, ***P < 0.001, ****P < 0.0001.
721

Supplemental Figures Legends

Extended Data Fig.1 | *C. parvum* intestinal infection burden in neonates with and without *C. parvum* infection.

a, Representative images of duodenum, jejunum and ileum sections from *C. parvum* infected and control mice immunostained for *C. parvum* and Ki67 (96 h p.i.). Blue: DAPI (nuclei), red: Ki67, green: *C. parvum*. Bars, 100 µm.

b, Relative amounts of mRNAs analysed by RT–qPCR. Neonatal mice (5 days old) were inoculated with *C. parvum* oocysts (10^6 oocysts per animal) for 96 h. Infection burden was evaluated by RT-qPCR of *cp18S* gene in the duodenum, jejunum and ileum, respectively. The cycle threshold (Ct) values were used to determine the infection burden.

Each symbol represents one mouse, all from the same litter. Statistical analysis: unpaired t test for b. Data is expressed as mean ± SEM, and representative of at least two independent experiments, n = 4 per group. *P < 0.05, **P < 0.01, ***P < 0.001, ****P < 0.0001.

Extended Data Fig.2 | *C. parvum* infection disrupts cholesterol homeostasis in the small intestine.

a, Differential gene expression analysis upon *C. parvum* infection (72 h p.i.). The enrichment of sterol esterase activity gene set is shown at the bottom.

b-d, GSEA showing the enriched pathways of inflammatory reactions (b), defense response (c), sterol homeostasis and sterol transport (d) (|NES| > 1, p < 0.05, FDR < 0.25).

e, g, h, Relative amounts of mRNAs analyzed by RT–qPCR. Gene expression was presented as fold change to uninfected control.

f, Immunoblotting analysis of proximal and ileal IECs samples. GAPDH and TUBULIN were used as loading control of cytosolic protein.

i, Small intestine length of control and *C. parvum* infected mice (120 h p.i.).

j, Sections from the proximal/Jejunum and distal small intestine of neonatal mice 4 days after *C. parvum* infection were immunostaining for Ki67 and *C. parvum*. Blue: DAPI (nuclei), red: Ki67, green: *C. parvum*.

Each symbol represents one mouse, all from the same litter. Statistical analysis: unpaired t test for (e, g-i). Data are expressed as mean ± SEM, and representative of at least two independent experiments, n = 3–5 per group. *P < 0.05, **P < 0.01, ***P < 0.001, ****P < 0.0001. For gel source data, see Supplementary Figure 1.

Extended Data Fig.3 | *C. parvum* infection alters hepatic genes expression.

a, Differential hepatic gene expression analysis upon *C. parvum* infection (72 h p.i.). The enrichment of positive regulation of immune response gene set is shown at the bottom.

b-f, Relative mRNA expression of lipid metabolic genes associated with the indicated processes were measured by RT-qPCR.

g, Immunoblotting analysis of liver samples in neonates with and without *C. parvum* infection (72 h p.i.). GAPDH and TUBULIN were used as loading control of cytosolic protein.

Each symbol represents one mouse, all from the same litter. Statistical analysis: unpaired t test for (b-f). Data are expressed as mean ± SEM, and representative of at least two independent experiments, n = 4–5 per group. *P < 0.05, **P < 0.01, ***P < 0.001, ****P < 0.0001. For gel source data, see Supplementary Figure 1.

Extended Data Fig.4 | Impaired lipid homeostasis in the livers of *C. parvum* infected mice.

a, Hierarchical clustering showing the similarity between control and *C. parvum* infected neonatal mice (96 h p.i.).
b, Volcano plot illustrating the hepatic lipids expression between control and *C. parvum* infected neonatal mice (96 h p.i.). Lipid with VIP ≥ 1 represents significant difference.
c, KEGG pathway enrichment analysis and differential abundance (DA) scores of differential metabolites in the liver of control and *C. parvum* infected neonatal mice (96 h p.i.). DA score = (up regulated lipids in a pathway-down regulated lipids in a pathway) / (Total number of lipids annotation in a pathway).
d, Oil Red O stains of the liver sections in neonates with and without *C. parvum* infection (96 h p.i.).
e, The total quantification of all hepatic lipids between control and *C. parvum* infected neonatal mice (96 h p.i.).
f-k, Graphs depicting quantification of the differences in hepatic BA (f), CE (g), Cholesterol (h), FFA (i), DG (j) and TG (k) between control or *C. parvum* infected mice (96 h p.i.).
l-n, Graphs showing the fold change of hepatic FFA (l), DG (m) and TG (n) with different chain lengths between control or *C. parvum* infected mice (96 h p.i.). Each point represents a lipid, the size of the point represents the P-value.
Each symbol represents one mouse, all from the same litter. Statistical analysis: unpaired t test for (e-k). Data are expressed as mean ± SEM, n = 4 per group. *P < 0.05, **P < 0.01, ***P < 0.001, ****P < 0.0001.

Extended Data Fig.5 | *C. parvum* infection alters intestinal lipid metabolic genes expression.
a-c, Relative amounts of mRNAs analyzed by RT–qPCR. Gene expression was presented as fold change to uninfected control.
d, Representative images of ileum (72 h and 96 h p.i.).
e, Immunoblot analysis of proximal and ileal IECs from control and *C. parvum* infected neonatal mice (72 h and 96 h p.i.). GAPDH was used as loading control of cytosolic protein.
f-h, GSEA showing the enriched pathways of fatty acid metabolic process (f), intestinal lipid absorption process (g) and vitamin metabolic process (h) (|NES| > 1, p < 0.05, FDR < 0.25).
Each symbol represents one mouse, all from the same litter. Statistical analysis: unpaired t test for (a-c). Data are expressed as mean ± SEM, and representative of at least two independent experiments, n = 3–4 per group. *P < 0.05, **P < 0.01, ***P < 0.001, ****P < 0.0001. For gel source data, see Supplementary Figure 1.

Extended Data Fig.6 | Impaired lipid homeostasis in the proximal IECs of *C. parvum* infected mice.
a, Graphs depicting quantification of the differences in proximal IECs lipid abundance of each subclass between control or *C. parvum* infected mice (96 h p.i.).
b, KEGG pathway enrichment analysis and DA scores of differential metabolites in proximal IECs of control and *C. parvum* infected neonatal mice (96 h p.i.).
c, Graphs showing the quantification of L-palmitoylcarnitine in proximal IECs between control or *C. parvum* infected mice (96 h p.i.).
d, Violin plot showing the result of top 18 differentially bile acids with the largest log2FC value. The box in the middle represents the interquartile range, and the middle box represents the 95% confidence interval. The black horizontal line is the median, and the outer shape represents the distribution density of the data.

Each symbol represents one mouse, all from the same litter. Statistical analysis: unpaired t test for (a,c). Data are expressed as mean ± SEM, and representative of at least two independent experiments, n = 3–4 per group. *P < 0.05, **P < 0.01, ***P < 0.001, ****P < 0.0001.

Extended Data Fig.7 | Effects of bile on *C. parvum* infection.

a, Effects of bile on *C. parvum* intestinal infection in neonates. Neonatal mice (5 days old) were orally administered *C. parvum* oocysts; PBS or bile were given at 24 h p.i. followed by daily for 4 days, respectively; Intestinal tissues were collected, and the mRNA levels of cholesterol biosynthesis genes (a) and cholesterol efflux genes (b) were measured by RT-qPCR. Gene expression was presented as fold change to uninfected control.

c, Immunofluorescent and Oil Red O staining of the distal small intestine sections from (a). A higher magnification of the boxed region (red) to visualize the *C. parvum* staining; Red arrow indicates *C. parvum* staining. Blue: DAPI, red: Ki67, green: *C. parvum*.

d, Effects of bile on *C. parvum* invasion of cultured HCT-8 cells. Cells were incubated with oocysts for 4 h in the presence of different concentrations of bile or PBS, followed by RT-qPCR of *cp18S*.

e, Effects of bile on *C. parvum* infection of 2D monolayers. Cells were incubated with oocysts for 4 h first, subsequently exposed to different concentration of bile or PBS for another 20 h, followed by RT-qPCR of *cp18S*.

Each symbol represents one mouse, all from the same litter. Statistical analysis: unpaired t test for (a, b, d, e). Data are expressed as mean ± SEM, and representative of at least two independent experiments, n = 4 per group. *P < 0.05, **P < 0.01, ***P < 0.001, ****P < 0.0001.

Extended Data Fig.8 | Effects of bile on HCT-8 cells viability with or without *C. parvum* infection.

a, Effects of bile on HCT-8 cells viability in the presence of *C. parvum* infection. Cells were incubated with oocysts for 4 h first, subsequently exposed to different concentrations of bile or PBS for another 20 h, followed by cell viability assay.

b, Cell survival of HCT-8 cells treated with different concentration of bile or PBS for 24 h.

(c, d) Cell survival of HCT-8 cells exposed to different concentration of bile or PBS with (c) or without (d) oocysts for 4 h. One-way analysis of variance (ANOVA) with Dunnett's multiple comparison test was used for correction of multiple comparisons in a-d, n = 4 per group. *P < 0.05, **P < 0.01, ***P < 0.001, ****P < 0.0001.

Extended Data Fig.9 | Bile intervention attenuates the dysregulated cell proliferation in crypts following *C. parvum* infection.

a, Neonatal mice (5 days old) were orally administered 1×10^5 *C. parvum* oocysts; PBS or bile was given at 24 h p.i. followed by daily for 3 days; Mice were i.p. injected with EdU and sacrificed at 4 h post injection. Representative images of Ki67, EdU staining of proliferating cells in crypts at 4 h post injection. Blue: DAPI (nuclei), red: Ki67, green: EdU. Bars, 50 μm.

References

1. Kotloff, K. L. *et al.* Burden and aetiology of diarrhoeal disease in infants and young children in developing countries (the Global Enteric Multicenter Study, GEMS): a prospective, case-control study. *Lancet Lond. Engl.* **382**, 209–222 (2013).
2. Checkley, W. *et al.* A review of the global burden, novel diagnostics, therapeutics, and vaccine targets for cryptosporidium. *Lancet Infect. Dis.* **15**, 85–94 (2015).
3. Sow, S. O. *et al.* The Burden of Cryptosporidium Diarrheal Disease among Children < 24 Months of Age in Moderate/High Mortality Regions of Sub-Saharan Africa and South Asia, Utilizing Data from the Global Enteric Multicenter Study (GEMS). *PLoS Negl. Trop. Dis.* **10**, e0004729 (2016).
4. Khalil, I. A. *et al.* Morbidity, mortality, and long-term consequences associated with diarrhoea from Cryptosporidium infection in children younger than 5 years: a meta-analyses study. *Lancet Glob. Health* **6**, e758–e768 (2018).
5. Costa, L. B. *et al.* Cryptosporidium-malnutrition interactions: mucosal disruption, cytokines, and TLR signaling in a weaned murine model. *J. Parasitol.* **97**, 1113–1120 (2011).
6. Kirkpatrick, B. D. *et al.* Cryptosporidiosis stimulates an inflammatory intestinal response in malnourished Haitian children. *J. Infect. Dis.* **186**, 94–101 (2002).
7. Mondal, D., Haque, R., Sack, R. B., Kirkpatrick, B. D. & Petri, W. A. Attribution of malnutrition to cause-specific diarrheal illness: evidence from a prospective study of preschool children in Mirpur, Dhaka, Bangladesh. *Am. J. Trop. Med. Hyg.* **80**, 824–826 (2009).
8. Tzipori, S. & Ward, H. Cryptosporidiosis: biology, pathogenesis and disease. *Microbes Infect.* **4**, 1047–1058 (2002).
9. Watson, A. J. M., Duckworth, C. A., Guan, Y. & Montrose, M. H. Mechanisms of epithelial cell shedding in the Mammalian intestine and maintenance of barrier function. *Ann. N. Y. Acad. Sci.* **1165**, 135–142 (2009).
10. Delgado, M. E., Grabinger, T. & Brunner, T. Cell death at the intestinal epithelial front line. *FEBS J.* **283**, 2701–2719 (2016).
11. Chen, X.-M., Keithly, J. S., Paya, C. V. & LaRusso, N. F. Cryptosporidiosis. *N. Engl. J. Med.* **346**, 1723–1731 (2002).
12. Pardy, R. D., Wallbank, B. A., Striepen, B. & Hunter, C. A. Immunity to Cryptosporidium: insights into principles of enteric responses to infection. *Nat. Rev. Immunol.* **24**, 142–155 (2024).
13. Wahlström, A., Sayin, S. I., Marschall, H.-U. & Bäckhed, F. Intestinal Crosstalk between Bile Acids and Microbiota and Its Impact on Host Metabolism. *Cell Metab.* **24**, 41–50 (2016).
14. Chiang, J. Y. L. Bile acids: regulation of synthesis. *J. Lipid Res.* **50**, 1955–1966 (2009).
15. Makishima, M. *et al.* Identification of a nuclear receptor for bile acids. *Science* **284**, 1362–1365 (1999).
16. Parks, D. J. *et al.* Bile acids: natural ligands for an orphan nuclear receptor. *Science* **284**, 1365–1368 (1999).
17. Forman, B. M. *et al.* Identification of a nuclear receptor that is activated by farnesol metabolites. *Cell* **81**, 687–693 (1995).
18. Matsubara, T., Li, F. & Gonzalez, F. J. FXR signaling in the enterohepatic system. *Mol. Cell. Endocrinol.* **368**, 17–29 (2013).
19. Marzook, N. B. *et al.* The essential host genome for Cryptosporidium survival exposes metabolic dependencies that can be leveraged for treatment. *Cell* S0092-8674(25)00751–2 (2025) doi:10.1016/j.cell.2025.07.001.
20. Ehrenman, K., Wanyiri, J. W., Bhat, N., Ward, H. D. & Coppens, I. Cryptosporidium parvum scavenges LDL-derived cholesterol and micellar cholesterol internalized into enterocytes. *Cell. Microbiol.* **15**, 1182–1197 (2013).
21. Deng, S. *et al.* Cryptosporidium uses CSpV1 to activate host type I interferon and attenuate antiparasitic defenses. *Nat. Commun.* **14**, 1456 (2023).
22. Luo, J., Yang, H. & Song, B.-L. Mechanisms and regulation of cholesterol homeostasis. *Nat. Rev. Mol. Cell Biol.* **21**, 225–245 (2020).
23. Wang, B. & Tontonoz, P. Liver X receptors in lipid signalling and membrane homeostasis. *Nat. Rev. Endocrinol.* **14**, 452–463 (2018).
24. Xu, D. *et al.* Cholesterol sulfate alleviates ulcerative colitis by promoting cholesterol biosynthesis in colonic epithelial cells. *Nat. Commun.* **13**, 4428 (2022).

910 25. Tso, P. & Balint, J. A. Formation and transport of chylomicrons by enterocytes to the lymphatics. *Am. J.*
911 *Physiol.* **250**, G715-726 (1986).
912 26. Ko, C.-W., Qu, J., Black, D. D. & Tso, P. Regulation of intestinal lipid metabolism: current concepts and
913 relevance to disease. *Nat. Rev. Gastroenterol. Hepatol.* **17**, 169–183 (2020).
914 27. Li, H., Yu, X.-H., Ou, X., Ouyang, X.-P. & Tang, C.-K. Hepatic cholesterol transport and its role in non-
915 alcoholic fatty liver disease and atherosclerosis. *Prog. Lipid Res.* **83**, 101109 (2021).
916 28. Jensen, R. G. Lipids in human milk. *Lipids* **34**, 1243–1271 (1999).
917 29. Liu, Z., Rochfort, S. & Cocks, B. Milk lipidomics: What we know and what we don't. *Prog. Lipid Res.* **71**, 70–
918 85 (2018).
919 30. Chen, F. *et al.* Liver receptor homologue-1 mediates species- and cell line-specific bile acid-dependent
920 negative feedback regulation of the apical sodium-dependent bile acid transporter. *J. Biol. Chem.* **278**, 19909–
921 19916 (2003).
922 31. Moschandrea, C. *et al.* Mitochondrial dysfunction abrogates dietary lipid processing in enterocytes.
923 *Nature* **625**, 385–392 (2024).
924 32. Spector, A. A. & Kim, H.-Y. Discovery of essential fatty acids. *J. Lipid Res.* **56**, 11–21 (2015).
925 33. Chen, X. M. & LaRusso, N. F. Mechanisms of attachment and internalization of Cryptosporidium parvum to
926 biliary and intestinal epithelial cells. *Gastroenterology* **118**, 368–379 (2000).
927 34. Feng, H., Nie, W., Sheoran, A., Zhang, Q. & Tzipori, S. Bile acids enhance invasiveness of Cryptosporidium
928 spp. into cultured cells. *Infect. Immun.* **74**, 3342–3346 (2006).
929 35. Fang, S. *et al.* Intestinal FXR agonism promotes adipose tissue browning and reduces obesity and insulin
930 resistance. *Nat. Med.* **21**, 159–165 (2015).
931 36. Fu, T. *et al.* FXR Regulates Intestinal Cancer Stem Cell Proliferation. *Cell* **176**, 1098-1112.e18 (2019).
932 37. Maran, R. R. M. *et al.* Farnesoid X receptor deficiency in mice leads to increased intestinal epithelial cell
933 proliferation and tumor development. *J. Pharmacol. Exp. Ther.* **328**, 469–477 (2009).
934 38. Modica, S., Murzilli, S., Salvatore, L., Schmidt, D. R. & Moschetta, A. Nuclear bile acid receptor FXR
935 protects against intestinal tumorigenesis. *Cancer Res.* **68**, 9589–9594 (2008).
936 39. Ming, Z., Zhou, R. & Chen, X.-M. Regulation of host epithelial responses to Cryptosporidium infection by
937 microRNAs. *Parasite Immunol.* **39**, (2017).
938 40. Thomson, S. *et al.* Bovine cryptosporidiosis: impact, host-parasite interaction and control strategies. *Vet.*
939 *Res.* **48**, 42 (2017).
940 41. Annaba, F. *et al.* Modulation of ileal bile acid transporter (ASBT) activity by depletion of plasma
941 membrane cholesterol: association with lipid rafts. *Am. J. Physiol. Gastrointest. Liver Physiol.* **294**, G489-497 (2008).
942 42. Cohen, D. E. Balancing cholesterol synthesis and absorption in the gastrointestinal tract. *J. Clin. Lipidol.* **2**,
943 S1-3 (2008).
944 43. Funkhouser-Jones, L. J. *et al.* Microbiota-produced indole metabolites disrupt mitochondrial function and
945 inhibit Cryptosporidium parvum growth. *Cell Rep.* **42**, 112680 (2023).
946 44. Kalantari, N. *et al.* Association between Cryptosporidium infection and cancer: A systematic review and
947 meta-analysis. *Parasitol. Int.* **74**, 101979 (2020).
948 45. Russler-Germain, E. V. *et al.* Commensal Cryptosporidium colonization elicits a cDC1-dependent Th1
949 response that promotes intestinal homeostasis and limits other infections. *Immunity* **54**, 2547-2564.e7 (2021).
950 46. Wallbank, B. A., Pardy, R. D., Brodsky, I. E., Hunter, C. A. & Striepen, B. Cryptosporidium impacts epithelial
951 turnover and is resistant to induced death of the host cell. *mBio* **15**, e0172024 (2024).
952 47. van Best, N. *et al.* Bile acids drive the newborn's gut microbiota maturation. *Nat. Commun.* **11**, 3692
953 (2020).
954 48. Fontaine, F., Turjeman, S., Callens, K. & Koren, O. The intersection of undernutrition, microbiome, and
955 child development in the first years of life. *Nat. Commun.* **14**, 3554 (2023).
956 49. VanDussen, K. L. *et al.* Neonatal Mouse Gut Metabolites Influence Cryptosporidium parvum Infection in
957 Intestinal Epithelial Cells. *mBio* **11**, e02582-20 (2020).
958 50. Charania, R., Wade, B. E., McNair, N. N. & Mead, J. R. Changes in the Microbiome of Cryptosporidium-
959 Infected Mice Correlate to Differences in Susceptibility and Infection Levels. *Microorganisms* **8**, 879 (2020).
960 51. Carey, M. A. *et al.* Megasphaera in the Stool Microbiota Is Negatively Associated With Diarrheal
961 Cryptosporidiosis. *Clin. Infect. Dis. Off. Publ. Infect. Dis. Soc. Am.* **73**, e1242–e1251 (2021).

962 52. Wang, Y. *et al.* Delivery of parasite Cdg7_Flc_0990 RNA transcript into intestinal epithelial cells during
963 Cryptosporidium parvum infection suppresses host cell gene transcription through epigenetic mechanisms. *Cell.*
964 *Microbiol.* **19**, (2017).
965 53. Ferguson, S. H. *et al.* Interferon-λ3 Promotes Epithelial Defense and Barrier Function Against
966 Cryptosporidium parvum Infection. *Cell. Mol. Gastroenterol. Hepatol.* **8**, 1–20 (2019).
967 54. Zhu, G. *et al.* Expression and functional characterization of a giant Type I fatty acid synthase (CpFAS1)
968 gene from Cryptosporidium parvum. *Mol. Biochem. Parasitol.* **134**, 127–135 (2004).
969 55. Chen, X.-M. *et al.* Cryptosporidium parvum invasion of biliary epithelia requires host cell tyrosine
970 phosphorylation of cortactin via c-Src. *Gastroenterology* **125**, 216–228 (2003).
971 56. Lacroix, S., Mancassola, R., Naciri, M. & Laurent, F. Cryptosporidium parvum-specific mucosal immune
972 response in C57BL/6 neonatal and gamma interferon-deficient mice: role of tumor necrosis factor alpha in
973 protection. *Infect. Immun.* **69**, 1635–1642 (2001).
974 57. Kapel, N. *et al.* Kinetics of mucosal ileal gamma-interferon response during cryptosporidiosis in
975 immunocompetent neonatal mice. *Parasitol. Res.* **82**, 664–667 (1996).
976 58. Yu, G., Wang, L.-G., Han, Y. & He, Q.-Y. clusterProfiler: an R package for comparing biological themes
977 among gene clusters. *Omics J. Integr. Biol.* **16**, 284–287 (2012).
978 59. Liberzon, A. *et al.* The Molecular Signatures Database (MSigDB) hallmark gene set collection. *Cell Syst.* **1**,
979 417–425 (2015).
980 60. Hänzelmann, S., Castelo, R. & Guinney, J. GSVA: gene set variation analysis for microarray and RNA-seq
981 data. *BMC Bioinformatics* **14**, 7 (2013).
982 61. Klomp, J. A. *et al.* Defining the KRAS- and ERK-dependent transcriptome in KRAS-mutant cancers. *Science*
983 **384**, eadk0775 (2024).
984 62. Yin, Q. *et al.* Enhancing milk quality and modulating rectal microbiota of dairy goats in starch-rich diet: the
985 role of bile acid supplementation. *J. Anim. Sci. Biotechnol.* **15**, 7 (2024).
986 63. Wang, J. *et al.* Identification and evaluation of a lipid-lowering small compound in preclinical models and
987 in a Phase I trial. *Cell Metab.* **34**, 667-680.e6 (2022).
988 64. Wang, B. *et al.* Phospholipid Remodeling and Cholesterol Availability Regulate Intestinal Stemness and
989 Tumorigenesis. *Cell Stem Cell* **22**, 206-220.e4 (2018).
990

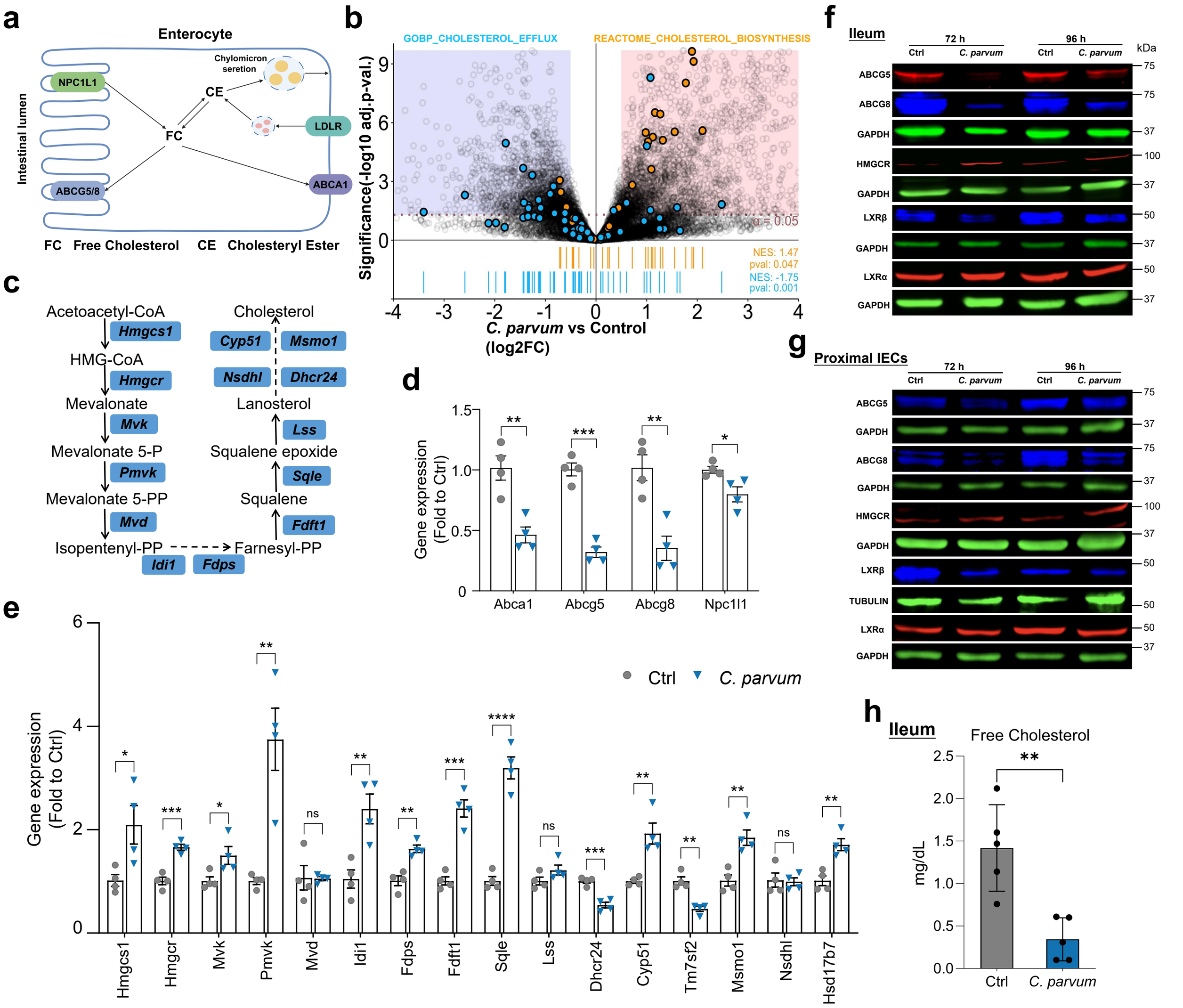
a
Enterocyte
Intestinal lumen
NPC1L1
Chylomicron seretion
CE
FC
LDLR
ABCG5/8
ABCA1
FC Free Cholesterol CE Cholesteryl Ester
b
GOBP_CHOLESTEROL_EFFLUX
REACTOME_CHOLESTEROL_BIOSYNTHESIS
Significance(-log10 adj.p-val.)
α = 0.05
NES: 1.47
pval: 0.047
NES: -1.75
pval: 0.001
C. parvum vs Control (log2FC)
c
Acetoacetyl-CoA
Hmgcs1
HMG-CoA
Hmgcr
Mevalonate
Mvk
Mevalonate 5-P
Pmvk
Mevalonate 5-PP
Mvd
Isopentenyl-PP
Idi1
Fdps
Farnesyl-PP
Fdft1
Squalene
Sqle
Squalene epoxide
Lss
Lanosterol
Dhcr24
Msmo1
Nsdhl
Cyp51
Cholesterol
d
Gene expression (Fold to Ctrl)
Abca1
Abcg5
Abcg8
Npc1l1
Ctrl
C. parvum
e
Gene expression (Fold to Ctrl)
Hmgcs1
Hmgcr
Mvk
Pmvk
Mvd
Idi1
Fdps
Fdft1
Sqle
Lss
Dhcr24
Cyp51
Tm7sf2
Msmo1
Nsdhl
Hsd17b7
f
Ileum
72 h
96 h
Ctrl
C. parvum
kDa
ABCG5
ABCG8
GAPDH
HMGCR
LXRβ
LXRα
g
Proximal IECs
TUBULIN
h
Ileum
Free Cholesterol
mg/dL
Ctrl
C. parvum

Fig. 1

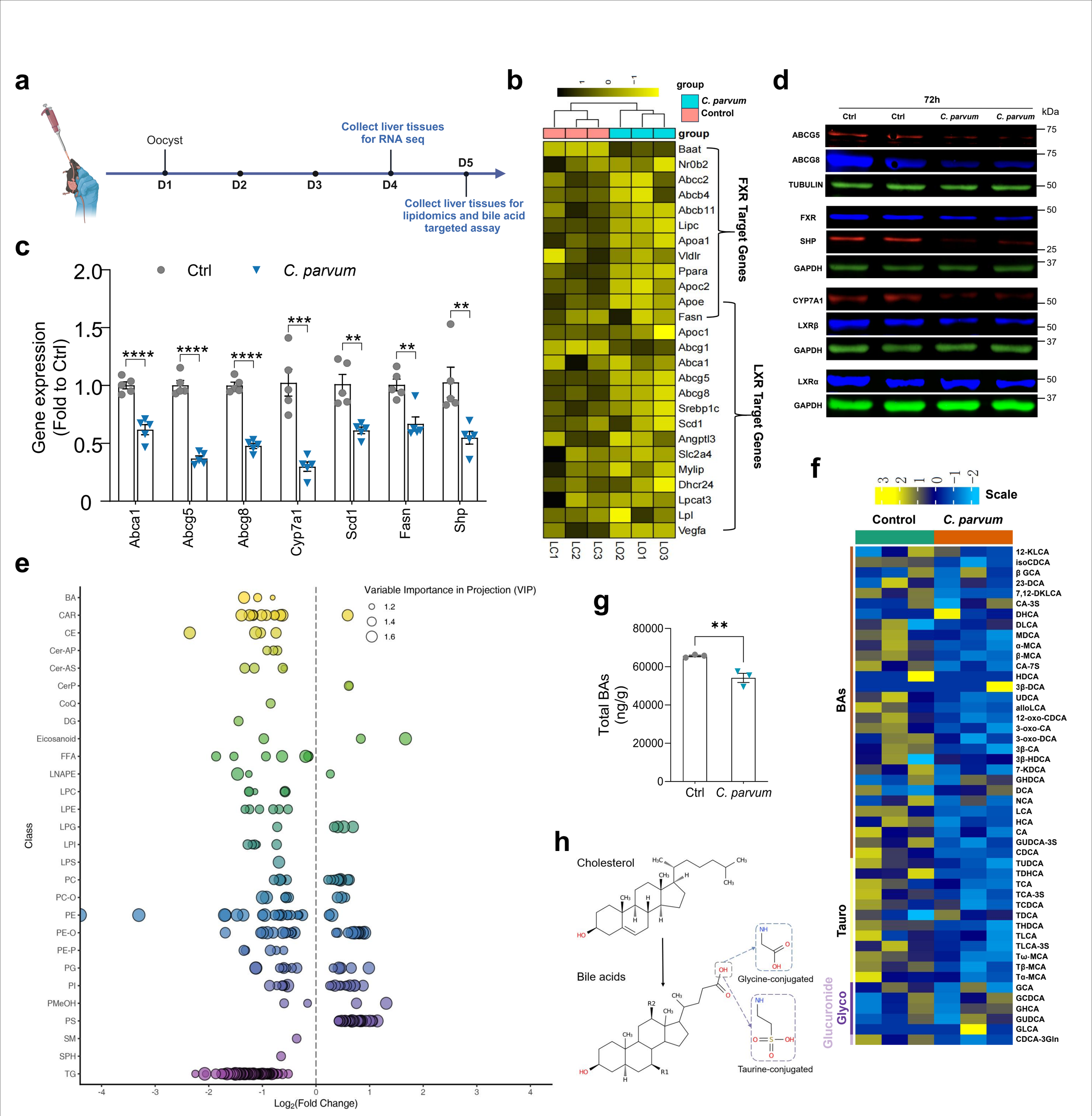
a
Oocyst
Collect liver tissues for RNA seq
D1
D2
D3
D4
D5
Collect liver tissues for lipidomics and bile acid targeted assay
b
group
C. parvum
Control
FXR Target Genes
LXR Target Genes
Baat
Nr0b2
Abcc2
Abcb4
Abcb11
Lipc
Apoa1
Vldlr
Ppara
Apoc2
Apoe
Fasn
Apoc1
Abcg1
Abca1
Abcg5
Abcg8
Srebp1c
Scd1
Angptl3
Slc2a4
Mylip
Dhcr24
Lpcat3
Lpl
Vegfa
LC1
LC2
LC3
LO2
LO1
LO3
c
Ctrl
C. parvum
Gene expression (Fold to Ctrl)
Abca1
Abcg5
Abcg8
Cyp7a1
Scd1
Fasn
Shp
d
72h
Ctrl
Ctrl
C. parvum
C. parvum
kDa
ABCG5
ABCG8
TUBULIN
FXR
SHP
GAPDH
CYP7A1
LXRβ
GAPDH
LXRα
GAPDH
e
Variable Importance in Projection (VIP)
Class
BA
CAR
CE
Cer-AP
Cer-AS
CerP
CoQ
DG
Eicosanoid
FFA
LNAPE
LPC
LPE
LPG
LPI
LPS
PC
PC-O
PE
PE-O
PE-P
PG
PI
PMeOH
PS
SM
SPH
TG
Log2(Fold Change)
f
Scale
Control
C. parvum
BAs
Tauro
Glucuronide
Glyco
12-KLCA
isoCDCA
β GCA
23-DCA
7,12-DKLCA
CA-3S
DHCA
DLCA
MDCA
α-MCA
β-MCA
CA-7S
HDCA
3β-DCA
UDCA
alloLCA
12-oxo-CDCA
3-oxo-CA
3-oxo-DCA
3β-CA
3β-HDCA
7-KDCA
GHDCA
DCA
NCA
LCA
HCA
CA
GUDCA-3S
CDCA
TUDCA
TDHCA
TCA
TCA-3S
TCDCA
TDCA
THDCA
TLCA
TLCA-3S
Tω-MCA
Tβ-MCA
Tα-MCA
GCA
GCDCA
GHCA
GUDCA
GLCA
CDCA-3Gln
g
Total BAs (ng/g)
Ctrl
C. parvum
h
Cholesterol
Bile acids
Glycine-conjugated
Taurine-conjugated

Fig. 2

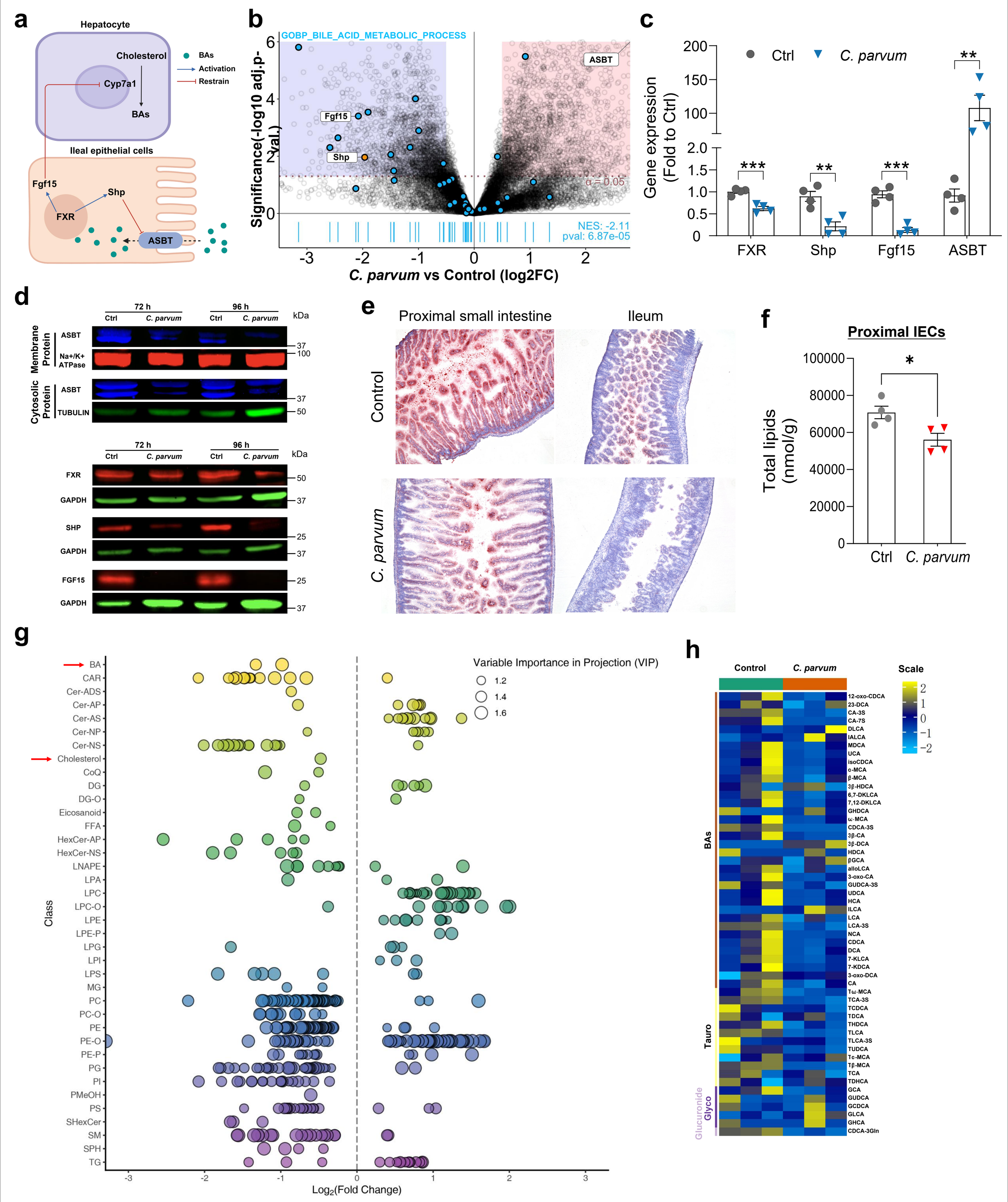
a
Hepatocyte
Cholesterol
Cyp7a1
BAs
BAs
Activation
Restrain
Ileal epithelial cells
Fgf15
Shp
FXR
ASBT
b
GOBP_BILE_ACID_METABOLIC_PROCESS
ASBT
Fgf15
Shp
α = 0.05
NES: -2.11
pval: 6.87e-05
Significance(-log10 adj.p-val.)
C. parvum vs Control (log2FC)
c
Ctrl
C. parvum
Gene expression (Fold to Ctrl)
FXR
Shp
Fgf15
ASBT
d
72 h
96 h
Ctrl
C. parvum
kDa
Membrane Protein
Cytosolic Protein
ASBT
Na+/K+ ATPase
TUBULIN
FXR
GAPDH
SHP
FGF15
e
Proximal small intestine
Ileum
Control
C. parvum
f
Proximal IECs
Total lipids (nmol/g)
Ctrl
C. parvum
g
Variable Importance in Projection (VIP)
Class
Log2(Fold Change)
h
Control
C. parvum
Scale
BAs
Tauro
Glycine
Glucuronide

Fig. 3

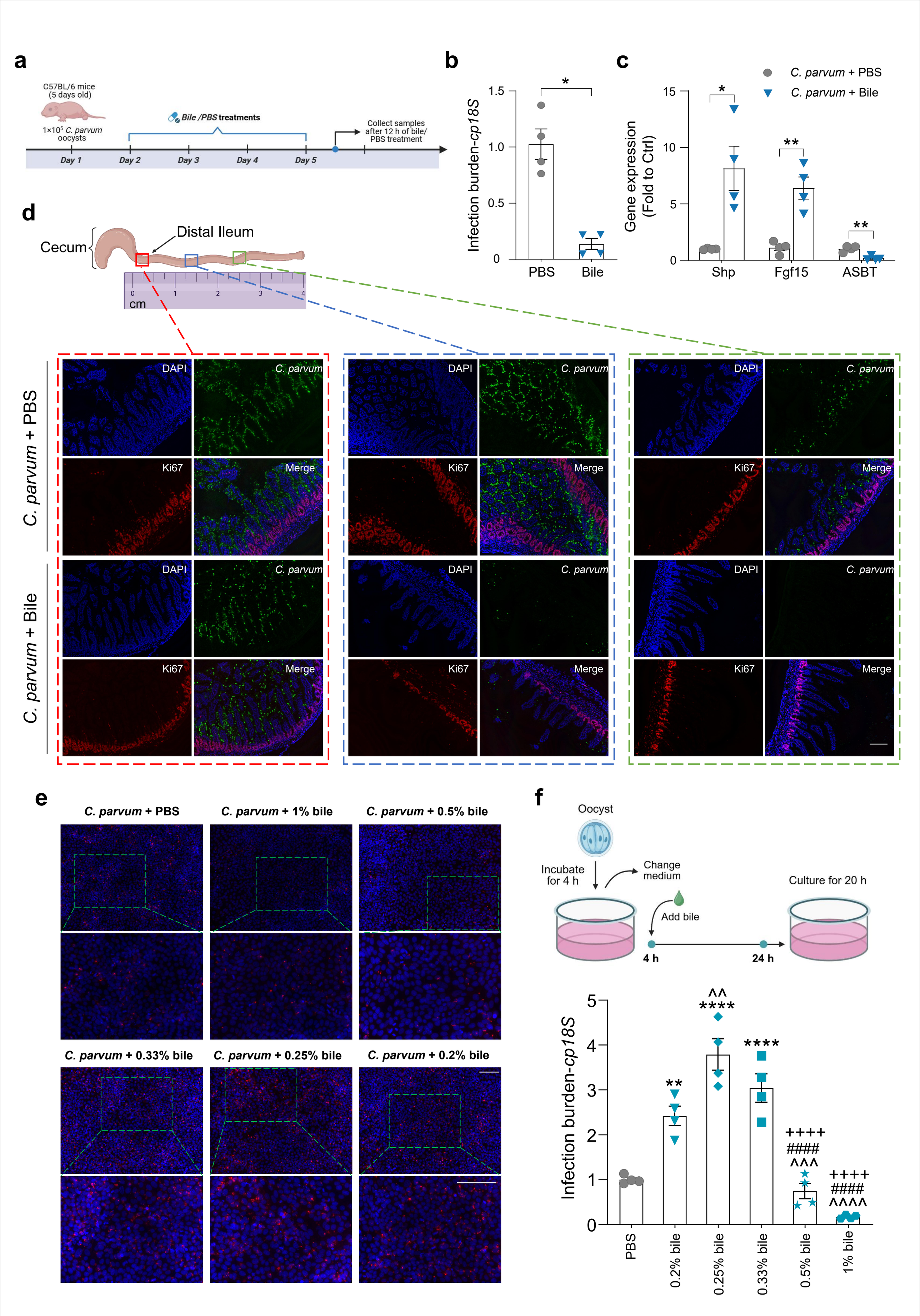
a
C57BL/6 mice
(5 days old)
1×10⁵ C. parvum
oocysts
Bile /PBS treatments
Collect samples
after 12 h of bile/
PBS treatment
Day 1
Day 2
Day 3
Day 4
Day 5
b
Infection burden-cp18S
PBS
Bile
c
C. parvum + PBS
C. parvum + Bile
Gene expression
(Fold to Ctrl)
Shp
Fgf15
ASBT
d
Cecum
Distal Ileum
cm
C. parvum + PBS
C. parvum + Bile
DAPI
C. parvum
Ki67
Merge
e
C. parvum + PBS
C. parvum + 1% bile
C. parvum + 0.5% bile
C. parvum + 0.33% bile
C. parvum + 0.25% bile
C. parvum + 0.2% bile
f
Oocyst
Incubate
for 4 h
Change
medium
Add bile
Culture for 20 h
4 h
24 h
Infection burden-cp18S
PBS
0.2% bile
0.25% bile
0.33% bile
0.5% bile
1% bile

Fig. 4

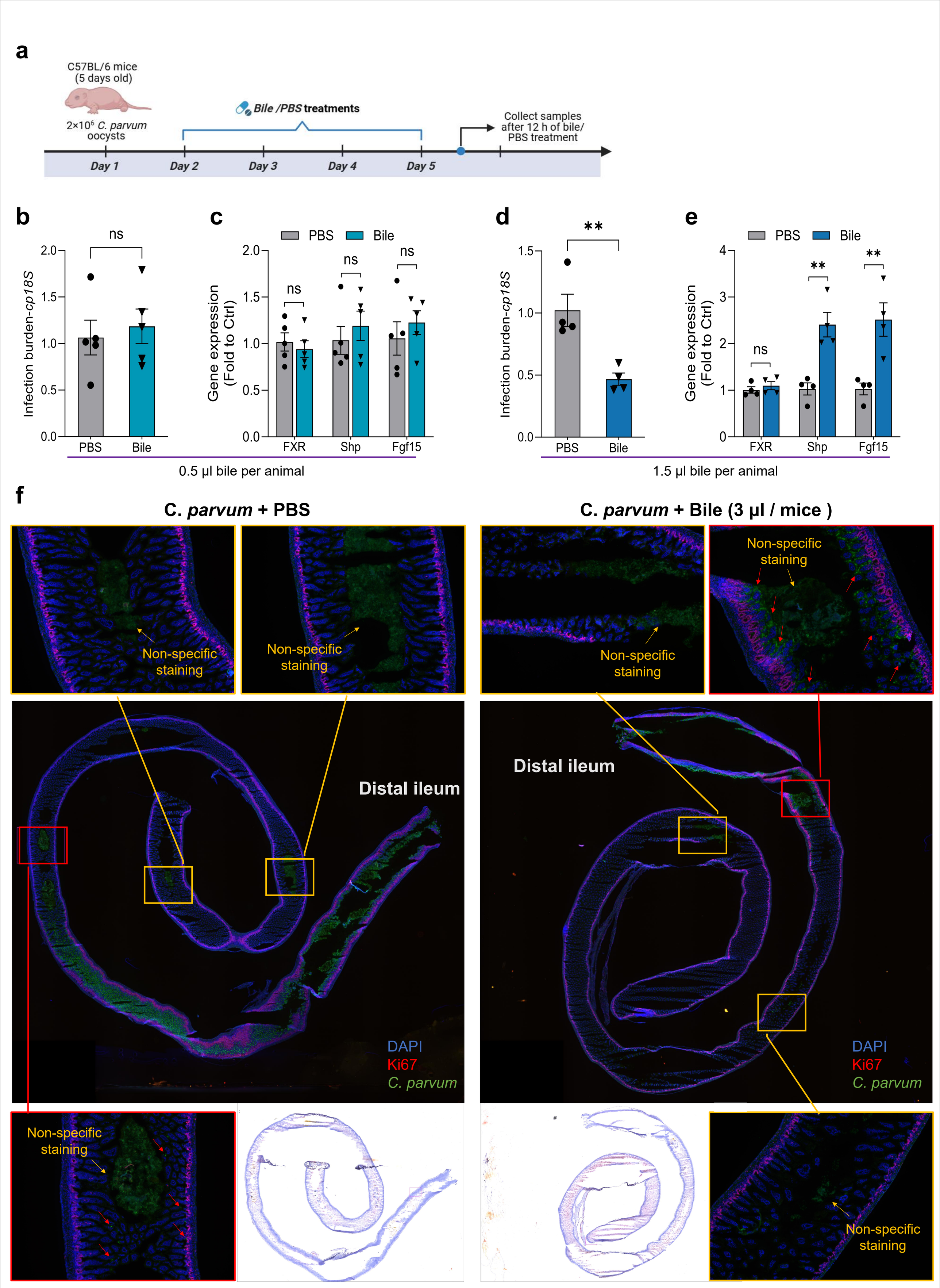
a
C57BL/6 mice
(5 days old)
2×10⁶ C. parvum
oocysts
Bile /PBS treatments
Collect samples
after 12 h of bile/
PBS treatment
Day 1
Day 2
Day 3
Day 4
Day 5
b
Infection burden-cp18S
ns
PBS
Bile
c
Gene expression
(Fold to Ctrl)
PBS
Bile
ns
ns
ns
FXR
Shp
Fgf15
0.5 µl bile per animal
d
Infection burden-cp18S
**
PBS
Bile
e
Gene expression
(Fold to Ctrl)
PBS
Bile
ns
**
**
FXR
Shp
Fgf15
1.5 µl bile per animal
f
C. parvum + PBS
C. parvum + Bile (3 µl / mice)
Non-specific
staining
Distal ileum
DAPI
Ki67
C. parvum

Fig. 5

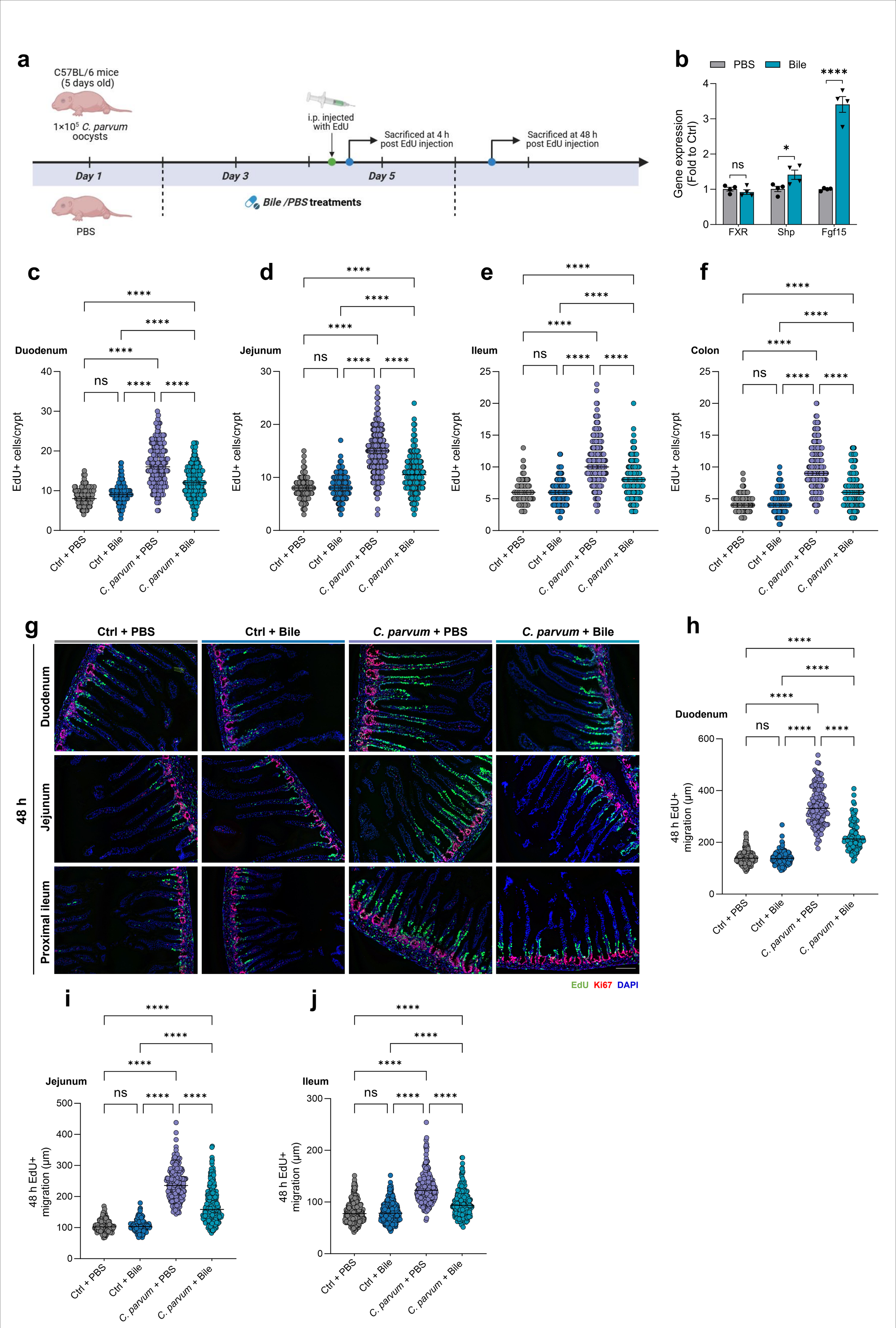
a
C57BL/6 mice
(5 days old)
1×10⁵ C. parvum
oocysts
i.p. injected
with EdU
Sacrificed at 4 h
post EdU injection
Sacrificed at 48 h
post EdU injection
Day 1
Day 3
Day 5
Bile /PBS treatments
PBS
b
PBS
Bile
Gene expression
(Fold to Ctrl)
FXR
Shp
Fgf15
c
Duodenum
d
Jejunum
e
Ileum
f
Colon
EdU+ cells/crypt
Ctrl + PBS
Ctrl + Bile
C. parvum + PBS
C. parvum + Bile
g
Ctrl + PBS
Ctrl + Bile
C. parvum + PBS
C. parvum + Bile
48 h
Duodenum
Jejunum
Proximal ileum
EdU Ki67 DAPI
h
Duodenum
48 h EdU+
migration (μm)
i
Jejunum
j
Ileum

Fig. 6

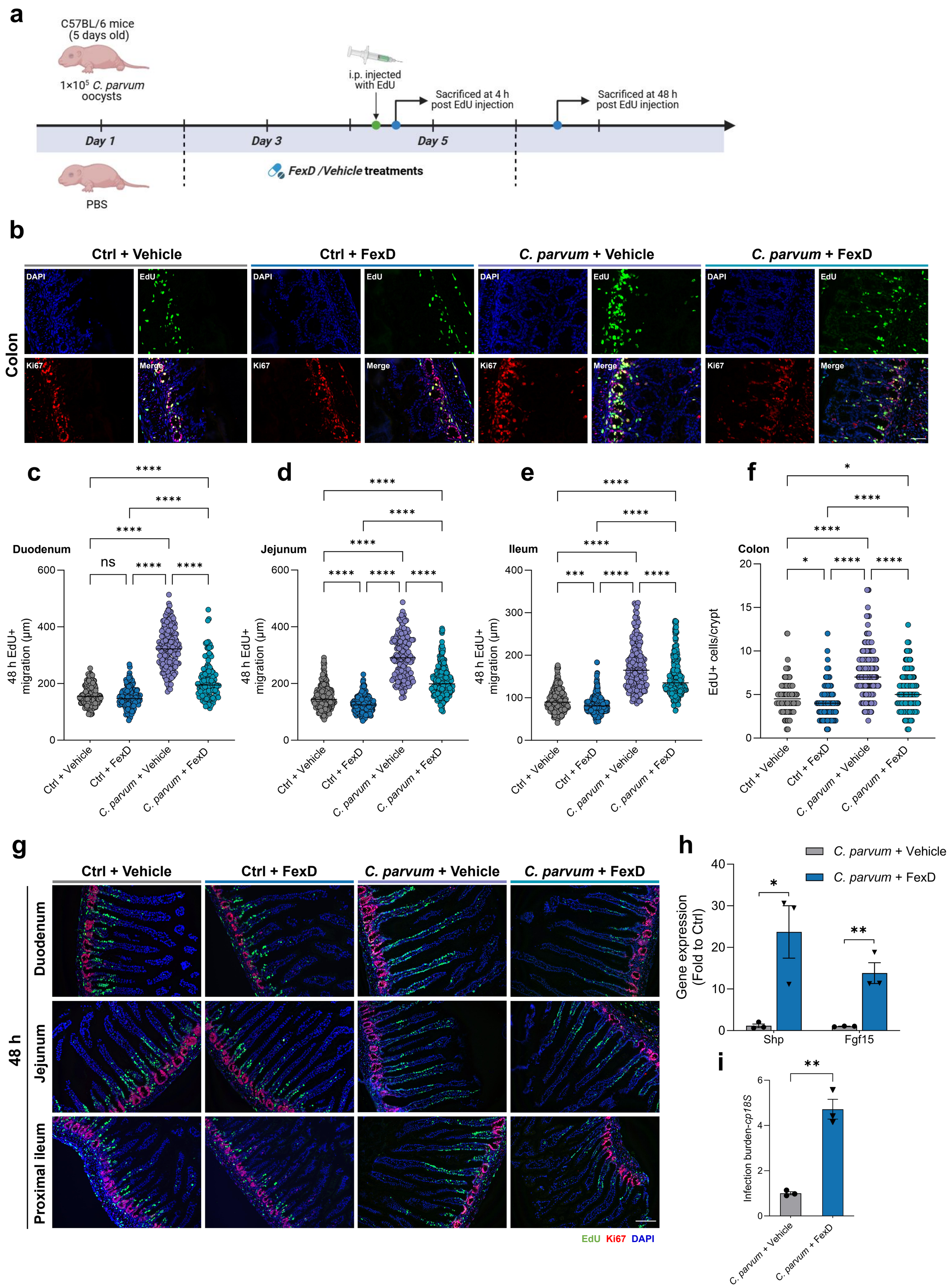
a
C57BL/6 mice
(5 days old)
1×10⁵ C. parvum
oocysts
i.p. injected
with EdU
Sacrificed at 4 h
post EdU injection
Sacrificed at 48 h
post EdU injection
Day 1
Day 3
Day 5
FexD /Vehicle treatments
PBS
b
Ctrl + Vehicle
Ctrl + FexD
C. parvum + Vehicle
C. parvum + FexD
Colon
DAPI
EdU
Ki67
Merge
c
Duodenum
48 h EdU+ migration (μm)
ns
****
d
Jejunum
e
Ileum
***
f
Colon
EdU+ cells/crypt
*
**
g
48 h
Duodenum
Jejunum
Proximal ileum
EdU Ki67 DAPI
h
C. parvum + Vehicle
C. parvum + FexD
Gene expression
(Fold to Ctrl)
Shp
Fgf15
i
Infection burden-cp18S

Fig. 7

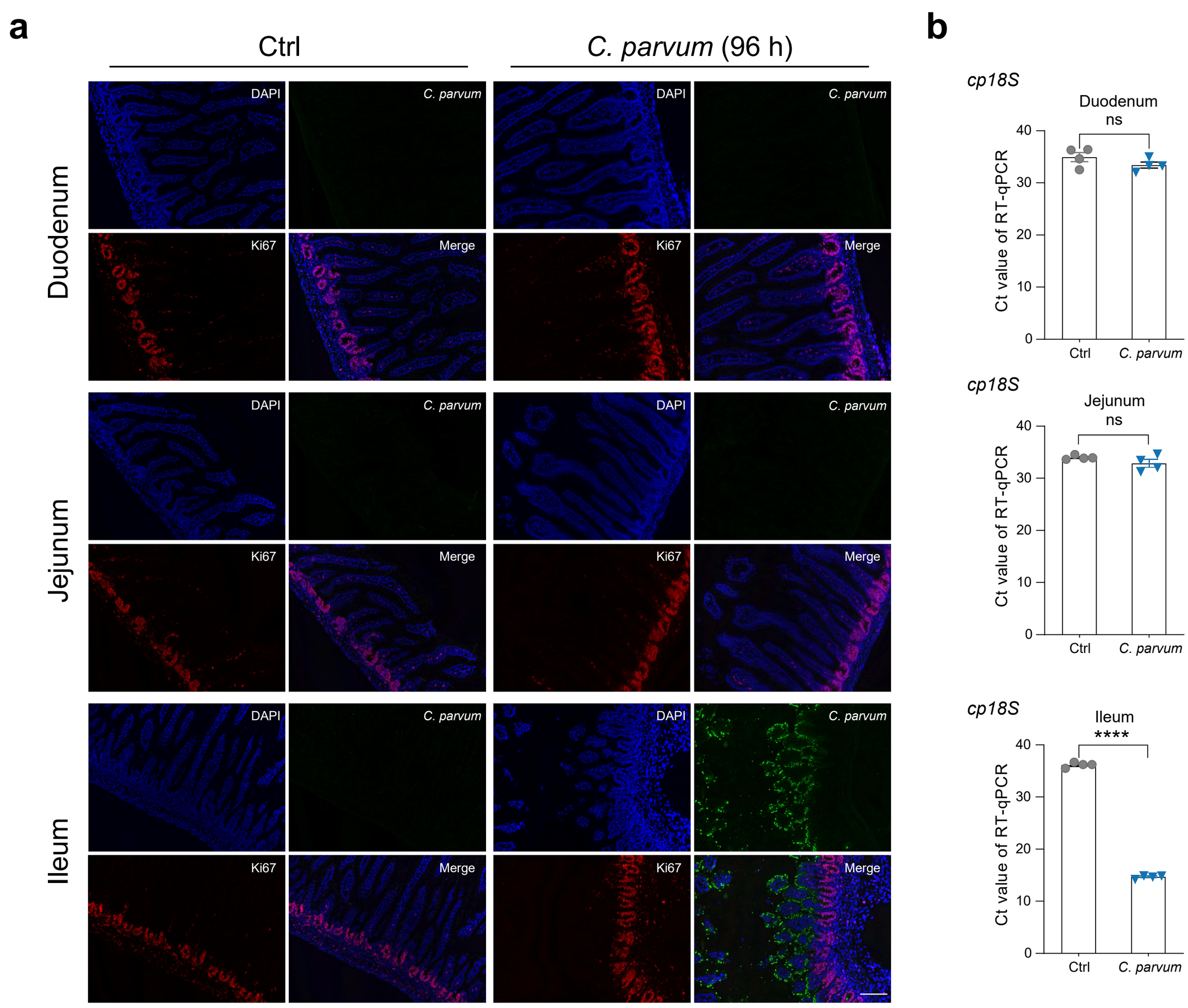

Extended Data Fig.1 | *C. parvum* intestinal infection burden in neonates with and without *C. parvum* infection.
a, Representative images of duodenum, jejunum and ileum sections from *C. parvum* infected and control mice immunostained for *C. parvum* and Ki67 (96 h p.i.). Blue: DAPI (nuclei), red: Ki67, green: *C. parvum*. Bars, 100 μm.
b, Relative amounts of mRNAs analysed by RT–qPCR. Neonatal mice (5 days old) were inoculated with *C. parvum* oocysts (10^6 oocysts per animal) for 96 h. Infection burden was evaluated by RT-qPCR of *cp18S* gene in the duodenum, jejunum and ileum, respectively. The cycle threshold (Ct) values were used to determine the infection burden.
Each symbol represents one mouse, all from the same litter. Statistical analysis: unpaired t test for b. Data is expressed as mean ± SEM, and representative of at least two independent experiments, n = 4 per group. *P < 0.05, **P < 0.01, ***P < 0.001, ****P < 0.0001.

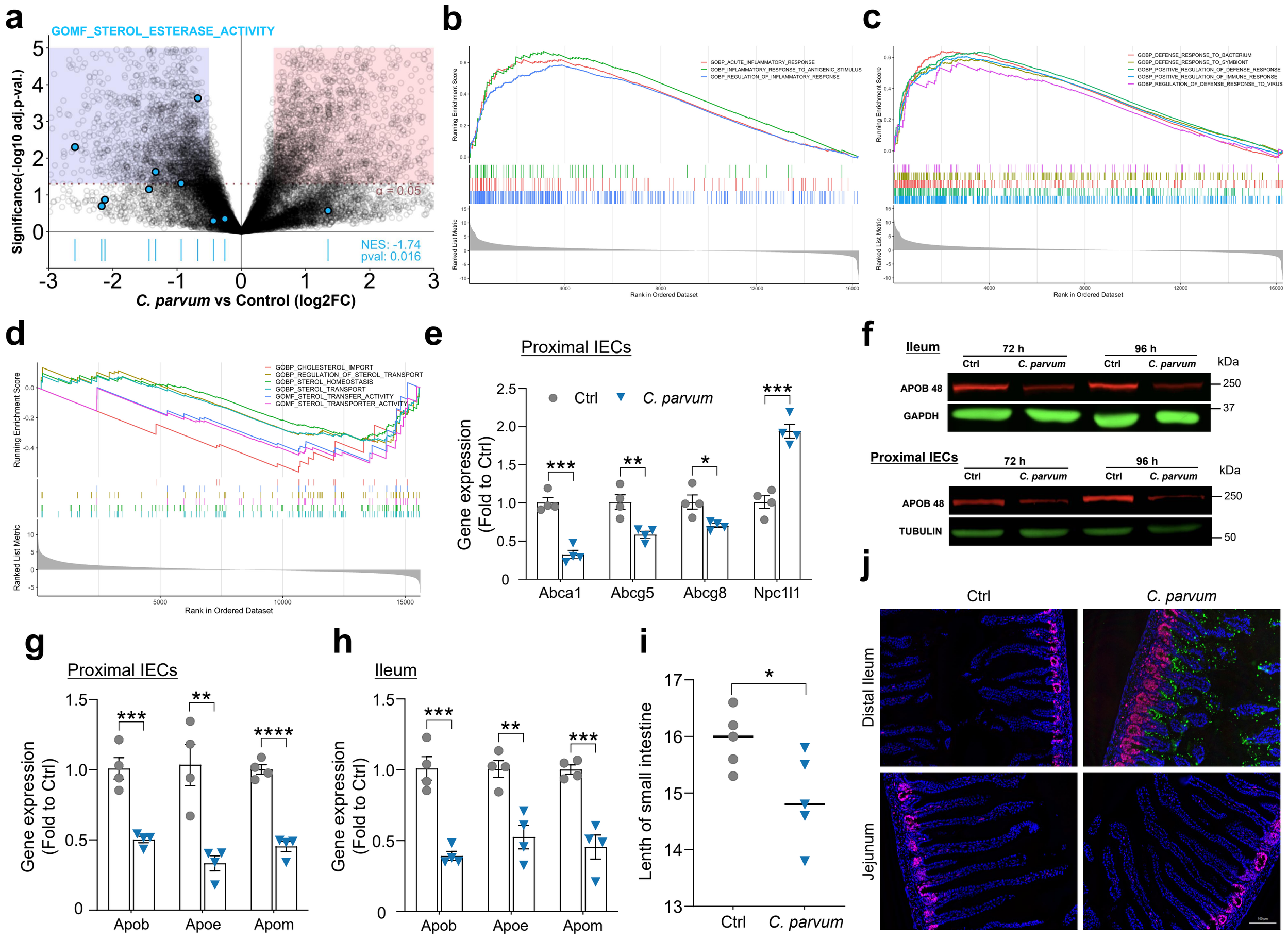

Extended Data Fig.2 | *C. parvum* infection disrupts cholesterol homeostasis in the small intestine.

a, Differential gene expression analysis upon *C. parvum* infection (72 h p.i.). The enrichment of sterol esterase activity gene set is shown at the bottom.

b-d, GSEA showing the enriched pathways of inflammatory reactions (b), defense response (c), sterol homeostasis and sterol transport (d) (|NES| > 1, $p < 0.05$, FDR < 0.25).

e, g, h, Relative amounts of mRNAs analyzed by RT–qPCR. Gene expression was presented as fold change to uninfected control.

f, Immunoblotting analysis of proximal and ileal IECs samples. GAPDH and TUBULIN were used as loading control of cytosolic protein.

i, Small intestine length of control and *C. parvum* infected mice (120 h p.i.).

j, Sections from the proximal/Jejunum and distal small intestine of neonatal mice 4 days after *C. parvum* infection were immunostaining for Ki67 and *C. parvum*. Blue: DAPI (nuclei), red: Ki67, green: *C. parvum*.

Each symbol represents one mouse, all from the same litter. Statistical analysis: unpaired t test for (e, g-i). Data are expressed as mean ± SEM, and representative of at least two independent experiments, n = 3–5 per group. *P < 0.05, **P < 0.01, ***P < 0.001, ****P < 0.0001. For gel source data, see Supplementary Figure 1

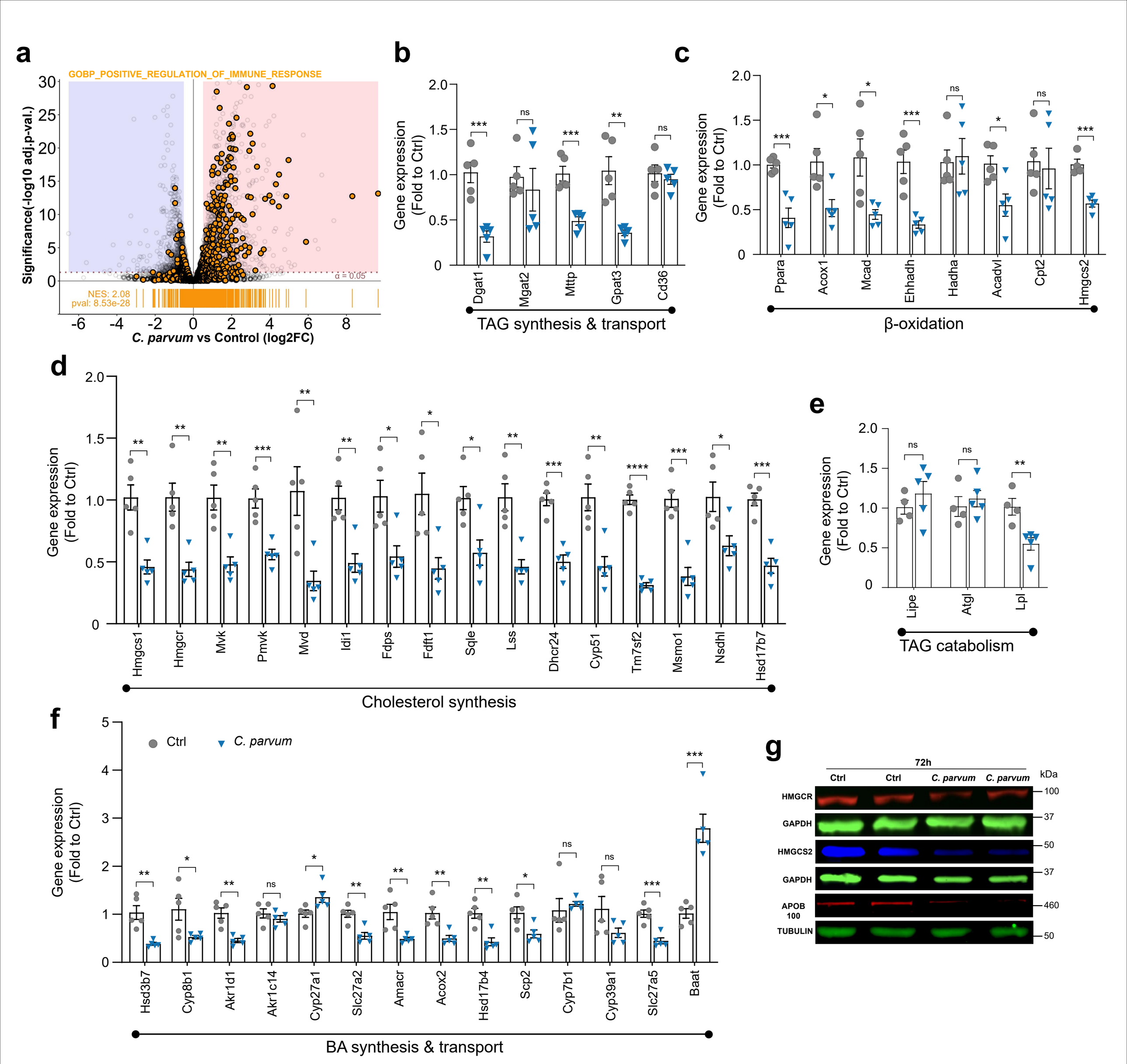

Extended Data Fig.3 | *C. parvum* infection alters hepatic genes expression.

a, Differential hepatic gene expression analysis upon *C. parvum* infection (72 h p.i.). The enrichment of positive regulation of immune response gene set is shown at the bottom.

b-f, Relative mRNA expression of lipid metabolic genes associated with the indicated processes were measured by RT-qPCR.

g, Immunoblotting analysis of liver samples in neonates with and without *C. parvum* infection (72 h p.i.). GAPDH and TUBULIN were used as loading control of cytosolic protein.

Each symbol represents one mouse, all from the same litter. Statistical analysis: unpaired t test for (b-f). Data are expressed as mean ± SEM, and representative of at least two independent experiments, n = 4–5 per group. *P < 0.05, **P < 0.01, ***P < 0.001, ****P < 0.0001. For gel source data, see Supplementary Figure 1.

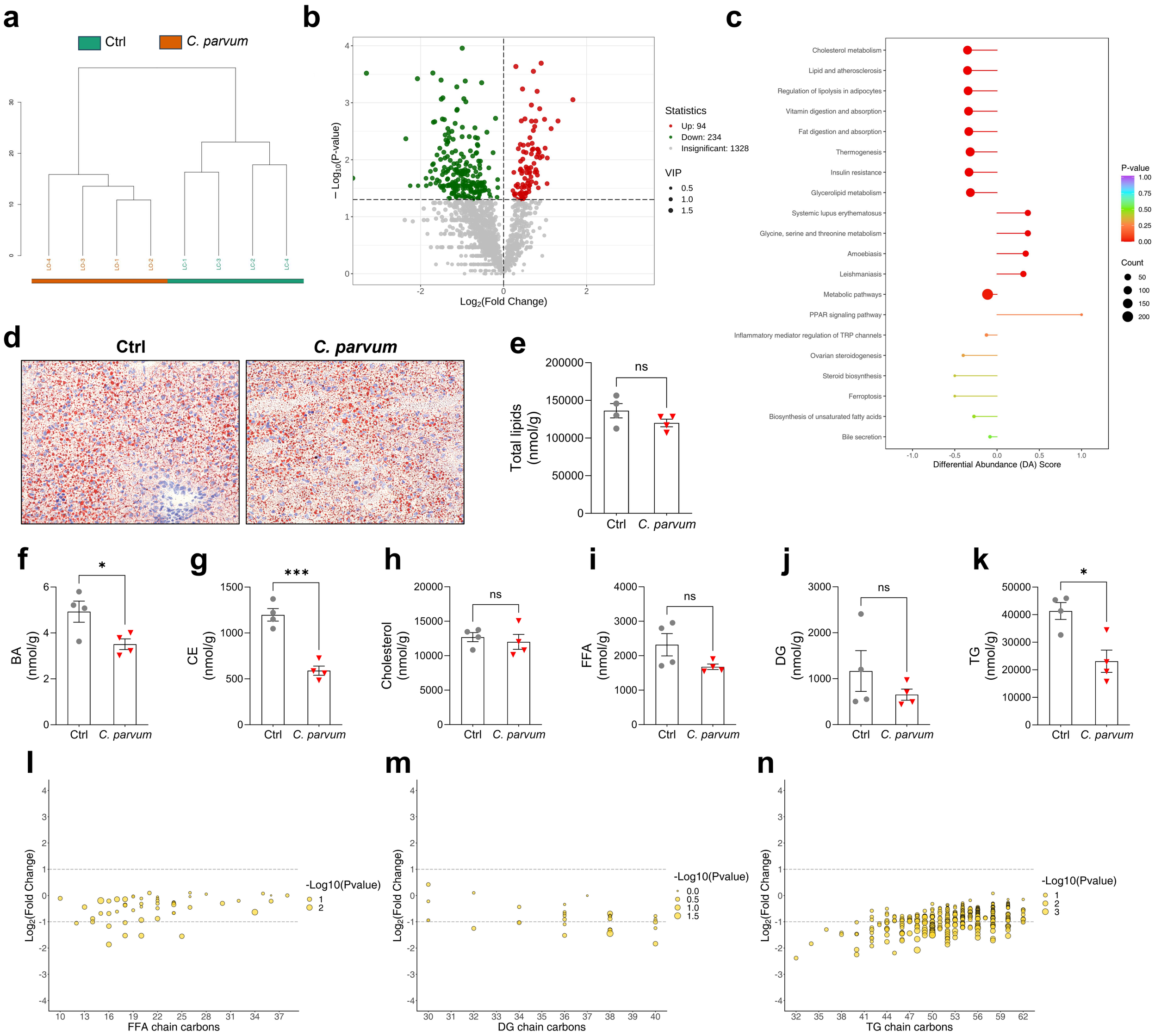

Extended Data Fig.4 | Impaired lipid homeostasis in the livers of *C. parvum* infected mice.

a, Hierarchical clustering showing the similarity between control and *C. parvum* infected neonatal mice (96 h p.i.).

b, Volcano plot illustrating the hepatic lipids expression between control and *C. parvum* infected neonatal mice (96 h p.i.). Lipid with VIP ≥ 1 represents significant difference.

c, KEGG pathway enrichment analysis and differential abundance (DA) scores of differential metabolites in the liver of control and *C. parvum* infected neonatal mice (96 h p.i.). DA score = (up regulated lipids in a pathway-down regulated lipids in a pathway) / (Total number of lipids annotation in a pathway).

d, Oil Red O stains of the liver sections in neonates with and without *C. parvum* infection (96 h p.i.).

e, The total quantification of all hepatic lipids between control and *C. parvum* infected neonatal mice (96 h p.i.).

f-k, Graphs depicting quantification of the differences in hepatic BA (f), CE (g), Cholesterol (h), FFA (i), DG (j) and TG (k) between control or *C. parvum* infected mice (96 h p.i.).

l-n, Graphs showing the fold change of hepatic FFA (l), DG (m) and TG (n) with different chain lengths between control or *C. parvum* infected mice (96 h p.i.). Each point represents a lipid, the size of the point represents the P-value.

Each symbol represents one mouse, all from the same litter. Statistical analysis: unpaired t test for (e-k). Data are expressed as mean ± SEM, n = 4 per group. *P < 0.05, **P < 0.01, ***P < 0.001, ****P < 0.0001.

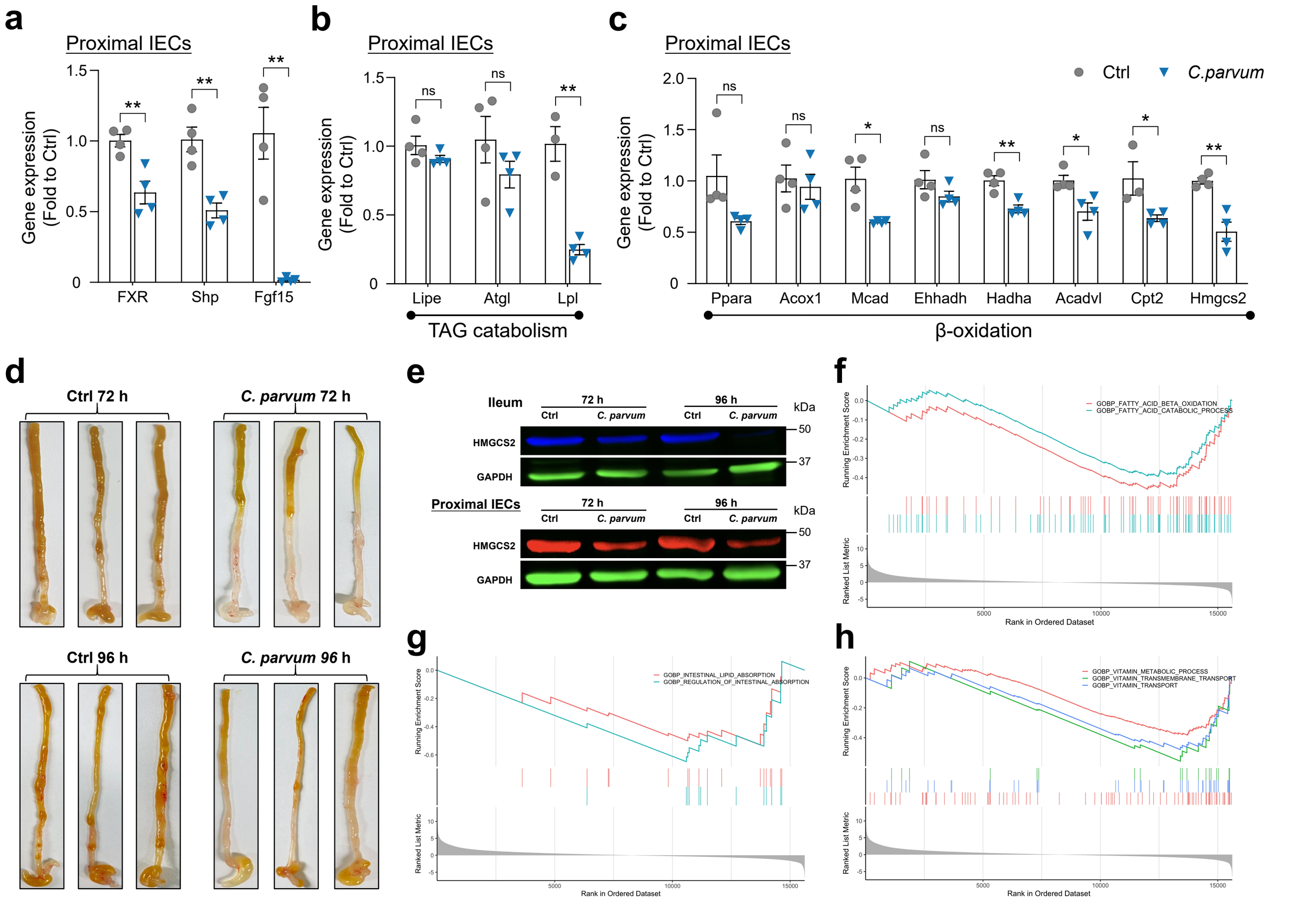

Extended Data Fig.5 | *C. parvum* infection alters intestinal lipid metabolic genes expression.

a-c, Relative amounts of mRNAs analyzed by RT–qPCR. Gene expression was presented as fold change to uninfected control.

d, Representative images of ileum (72 h and 96 h p.i.).

e, Immunoblot analysis of proximal and ileal IECs from control and *C. parvum* infected neonatal mice (72 h and 96 h p.i.). GAPDH was used as loading control of cytosolic protein.

f-h, GSEA showing the enriched pathways of fatty acid metabolic process (f), intestinal lipid absorption process (g) and vitamin metabolic process (h) (|NES| > 1, p < 0.05, FDR < 0.25).

Each symbol represents one mouse, all from the same litter. Statistical analysis: unpaired t test for (a-c). Data are expressed as mean ± SEM, and representative of at least two independent experiments, n = 3–4 per group. *P < 0.05, **P < 0.01, ***P < 0.001, ****P < 0.0001. For gel source data, see Supplementary Figure 1.

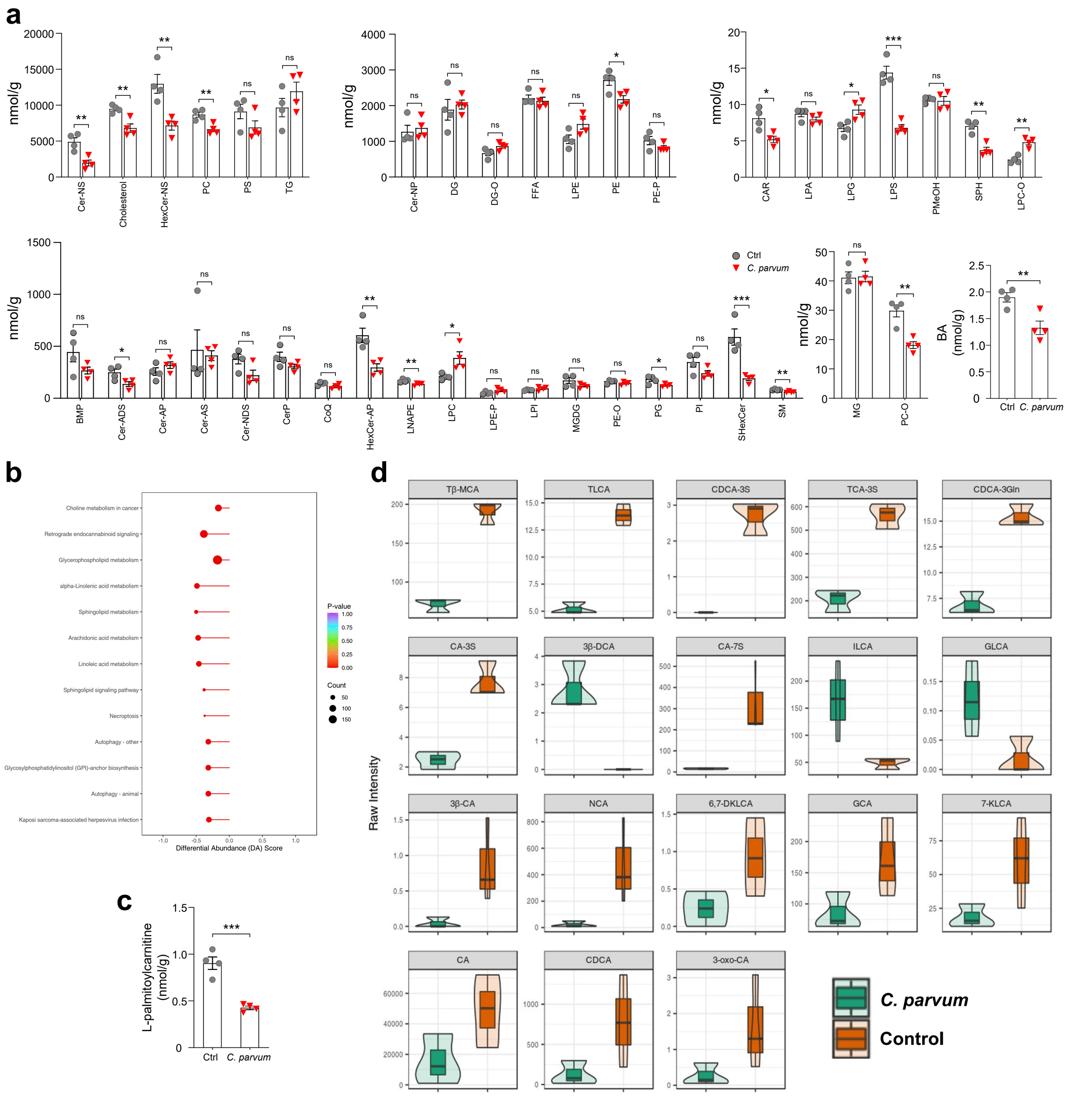

Extended Data Fig.6 | Impaired lipid homeostasis in the proximal IECs of *C. parvum* infected mice.
a, Graphs depicting quantification of the differences in proximal IECs lipid abundance of each subclass between control or *C. parvum* infected mice (96 h p.i.).
b, KEGG pathway enrichment analysis and DA scores of differential metabolites in proximal IECs of control and *C. parvum* infected neonatal mice (96 h p.i.).
c, Graphs showing the quantification of L-palmitoylcarnitine in proximal IECs between control or *C. parvum* infected mice (96 h p.i.).
d, Violin plot showing the result of top 18 differentially bile acids with the largest log2FC value. The box in the middle represents the interquartile range, and the middle box represents the 95% confidence interval. The black horizontal line is the median, and the outer shape represents the distribution density of the data. Each symbol represents one mouse, all from the same litter. Statistical analysis: unpaired t test for (a,c). Data are expressed as mean ± SEM, and representative of at least two independent experiments, n = 3–4 per group. *P < 0.05, **P < 0.01, ***P < 0.001, ****P < 0.0001.

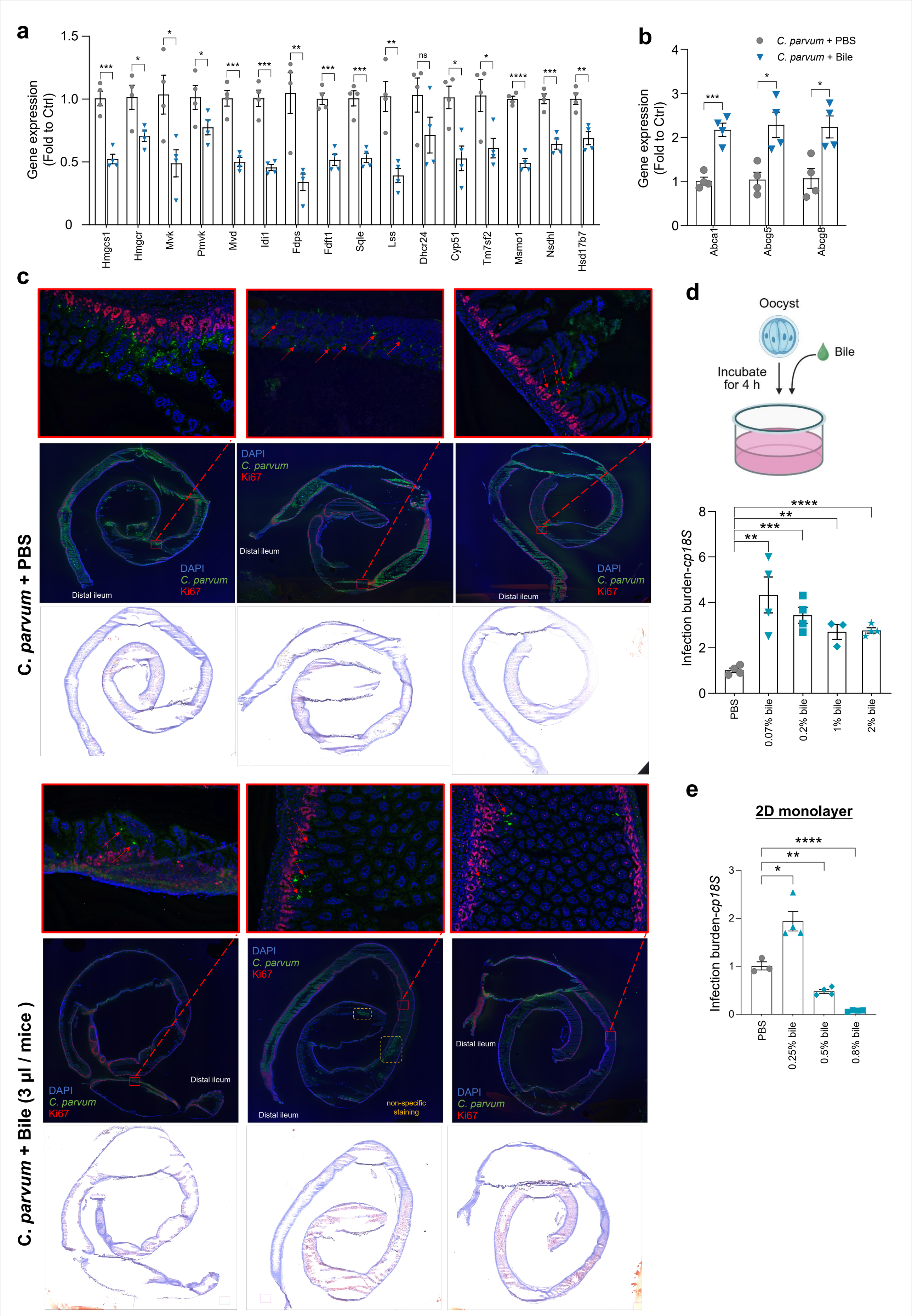

Extended Data Fig.7 | Effects of bile on *C. parvum* infection.

a, Effects of bile on *C. parvum* intestinal infection in neonates. Neonatal mice (5 days old) were orally administered *C. parvum* oocysts; PBS or bile were given at 24 h p.i. followed by daily for 4 days, respectively; Intestinal tissues were collected, and the mRNA levels of cholesterol biosynthesis genes (a) and cholesterol efflux genes (b) were measured by RT-qPCR. Gene expression was presented as fold change to uninfected control.

c, Immunofluorescent and Oil Red O staining of the distal small intestine sections from (a). A higher magnification of the boxed region (red) to visualize the *C. parvum* staining; Red arrow indicates *C. parvum* staining. Blue: DAPI, red: Ki67, green: *C. parvum*.

d, Effects of bile on *C. parvum* invasion of cultured HCT-8 cells. Cells were incubated with oocysts for 4 h in the presence of different concentrations of bile or PBS, followed by RT-qPCR of *cp18S*.

e, Effects of bile on *C. parvum* infection of 2D monolayers. Cells were incubated with oocysts for 4 h first, subsequently exposed to different concentration of bile or PBS for another 20 h, followed by RT-qPCR of *cp18S*.

Each symbol represents one mouse, all from the same litter. Statistical analysis: unpaired t test for (a, b, d, e). Data are expressed as mean ± SEM, and representative of at least two independent experiments, n = 4 per group. *P < 0.05, **P < 0.01, ***P < 0.001, ****P < 0.0001.

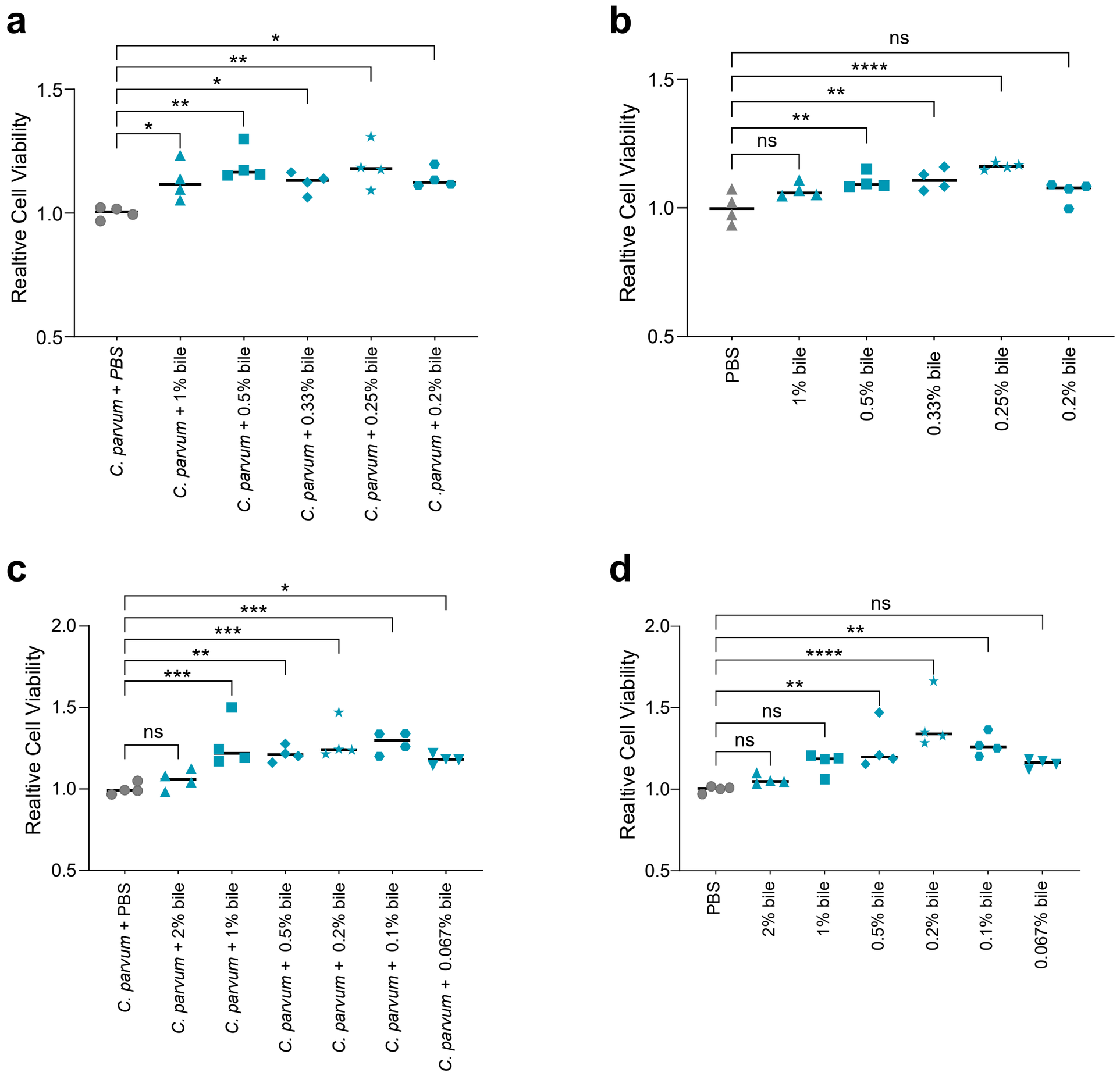

Extended Data Fig.8 | Effects of bile on HCT-8 cells viability with or without *C. parvum* infection.
a, Effects of bile on HCT-8 cells viability in the presence of *C. parvum* infection. Cells were incubated with oocysts for 4 h first, subsequently exposed to different concentrations of bile or PBS for another 20 h, followed by cell viability assay.
b, Cell survival of HCT-8 cells treated with different concentration of bile or PBS for 24 h.
(c, d) Cell survival of HCT-8 cells exposed to different concentration of bile or PBS with (c) or without (d) oocysts for 4 h. One-way analysis of variance (ANOVA) with Dunnett's multiple comparison test was used for correction of multiple comparisons in a-d, n = 4 per group. *P < 0.05, **P < 0.01, ***P < 0.001, ****P < 0.0001.

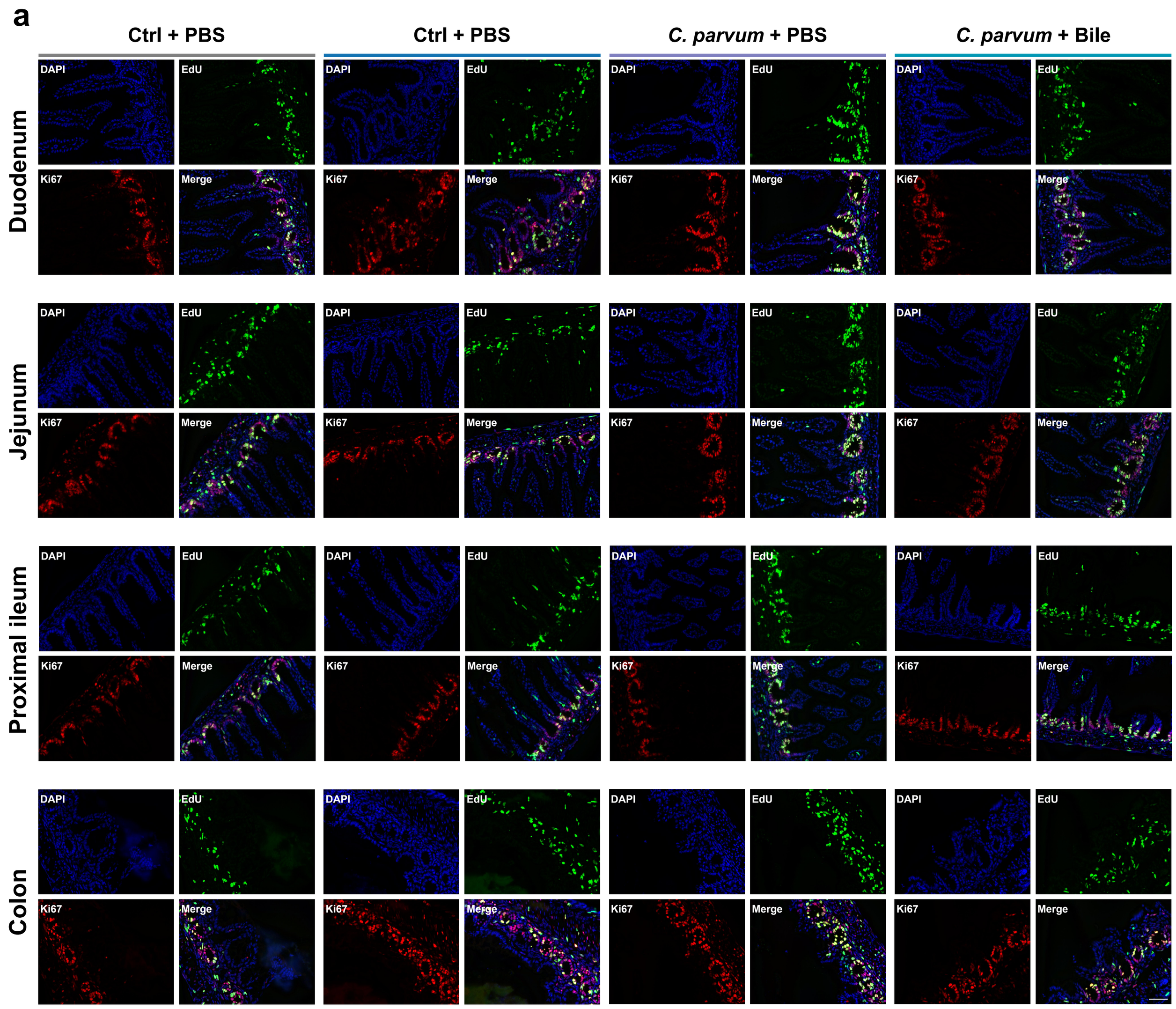

Extended Data Fig.9 | Bile intervention attenuates the dysregulated cell proliferation in crypts following *C. parvum* infection. **a,** Neonatal mice (5 days old) were orally administered 1×10^5 *C. parvum* oocysts; PBS or bile was given at 24 h p.i. followed by daily for 3 days; Mice were i.p. injected with EdU and sacrificed at 4 h post injection. Representative images of Ki67, EdU staining of proliferating cells in crypts at 4 h post injection. Blue: DAPI (nuclei), red: Ki67, green: EdU. Bars, 50 μm.